Monthly Notices of the ROYAL ASTRONOMICAL SOCIETY
MNRAS **548,** 1–19 (2026) https://doi.org/10.1093/mnras/staf2109

A black hole in a near pristine galaxy 700 Myr after the big bang

Roberto Maiolino [1,2,3★] Hannah Übler [4] Francesco D'Eugenio,[1,2] Jan Scholtz,[1,2] Ignas Juodžbalis,[1,2] Xihan Ji [1,2] Michele Perna,[5] Volker Bromm,[6,7] Pratika Dayal,[8] Sophie Koudmani [9,10,11,12] Boyuan Liu [10,13] Raffaella Schneider [14,15,16,17] Debora Sijacki,[1,10] Rosa Valiante [15,16] Alessandro Trinca [15,16,18] Saiyang Zhang [6,7] Marta Volonteri,[19] Kohei Inayoshi,[20] Stefano Carniani [21] Kimihiko Nakajima [22] Yuki Isobe [1,2,23] Joris Witstok,[24,25] Gareth C. Jones [1,2] Sandro Tacchella [1,2] Santiago Arribas,[5] Andrew Bunker,[26] Elisa Cataldi,[27,28,29] Stephane Charlot [19] Giovanni Cresci Mirko Curti,[27] Andrew C. Fabian [10] Harley Katz,[30,31] Nimisha Kumari [32] Nicolas Laporte [33] Giovanni Mazzolari,[4] Brant Robertson,[34] Fengwu Sun,[35] Bruno Rodriguez Del Pino[5] and Giacomo Venturi [22]

Affiliations are listed at the end of the paper

Accepted 2025 November 19. Received 2025 November 19; in original form 2025 September 17

ABSTRACT

The recent discovery of a large number of massive black holes within the first two billion years after the big bang, as well as their peculiar properties, have been largely unexpected based on the extrapolation of the properties of luminous quasars. These findings have prompted the development of several theoretical models for the early formation and growth of black holes, which are, however, difficult to differentiate. We report the metallicity measurement around a gravitationally lensed massive black hole at redshift 7.04 (classified as a Little Red Dot), hosted in a galaxy with very low dynamical mass. The weakness of the [O III]5007 emission line relative to the narrow Hβ emission indicates extremely low metallicity, about 4×10^{-3} solar, and even more metal poor in the surrounding few 100 pc. We argue that such properties cannot be uncommon among accreting black holes around this early cosmic epoch. Explaining such a low chemical enrichment in a system that has developed a massive black hole is challenging for most theories. Models assuming heavy black hole seeds (such as Direct Collapse Black Holes) or super-Eddington accretion scenarios struggle to explain the observations, although they can potentially reproduce the observed properties in some cases. Models invoking 'primordial black holes' (i.e. putative black holes formed shortly after the big bang) may potentially explain the low chemical enrichment associated with this black hole, although this class of models also requires further developments for proper testing.

Key words: galaxies: active – galaxies: formation – galaxies: high-redshift – galaxies: nuclei – quasars: emission lines.

1 INTRODUCTION

The *James Webb Space Telescope* (*JWST*) has opened a new window on the exploration of the formation and evolution of black holes (BHs) in the early universe. Indeed, *JWST*'s unprecedented sensitivity and wavelength coverage has enabled the detection of active galactic nuclei (AGNs) at high redshift that have luminosities much lower than quasars discovered from ground-based surveys, and also pushing the AGN discovery frontier to much higher redshifts (e.g. Y. Harikane et al. 2023; D. D. Kocevski et al. 2023; V. Kokorev et al. 2023; J. Matthee et al. 2024; H. Übler et al. 2023; J. Chisholm et al. 2024; L. J. Furtak et al. 2024; J. E. Greene et al. 2024; A. J. Taylor et al. 2025a, b; R. Tripodi et al. 2024; I. Juodžbalis et al. 2024b, 2025a; R. Maiolino et al. 2024a, b; G. Mazzolari et al. 2025; S. Geris et al. 2025; J. Scholtz et al. 2025). These AGNs are typically identified through a broad component of the permitted lines (typically Hα or Hβ), without a counterpart in [O III] (hence ascribing them to the broad-line regions (BLRs) of AGN rather than outflows), as well as high excitation lines typical of the hard and intense radiation field of AGN. The low luminosity of these *JWST*-discovered AGN is partly due to lower BH masses and/or lower accretion rates (I. Juodžbalis et al. 2024b; R. Maiolino et al. 2024b; I. Juodžbalis et al. 2025a). However, these lower luminosity AGN are not simply the high-redshift version of AGN known locally or at intermediate redshifts, and neither are scaled down version of quasars at similarly high redshifts. The new population of AGN discovered by *JWST* seems to be quite different from the AGN populations previously known. Indeed, they are found to be extremely X-ray weak (T. T. Ananna et al. 2024; M. Yue et al. 2024; R. Maiolino et al. 2025) and radio weak (G. Mazzolari et al. 2024a, 2025). They also typically show weak or no variability (M. Kokubo & Y. Harikane 2024; L. J. Furtak et al. 2025; R. P. Naidu et al. 2025; Z. Zhang et al. 2025; X. Ji et al. 2025a). Most of them appear to be overmassive in terms of BH-to-stellar

★ E-mail: rm665@cam.ac.uk

mass ratio, relative to the local relation (Y. Harikane et al. 2023; L. J. Furtak et al. 2024; I. Juodžbalis et al. 2024b, 2025a; R. Maiolino et al. 2024b; C.-H. Chen et al. 2025). Although part of this overmassive nature is certainly due to selection effects (J. Li et al. 2025; S. Geris et al. 2025; I. Juodžbalis et al. 2025a), it is still remarkable that some of these AGN have BHs that are nearly as massive as their host galaxies. Many of these new AGN lack strong high-ionization lines (e.g. E. Lambrides et al. 2024) as well as the classical iron emission bumps (B. Trefoloni et al. 2025; X. Ji et al. 2025c). They are also exceptionally nitrogen-rich (Y. Isobe et al. 2025). Multiple models have been suggested to interpret these results, ranging from high (super-Eddington, SE) accretion rates (R. Schneider et al. 2023; P. Madau & F. Haardt 2024; F. Pacucci & R. Narayan 2024; R. Maiolino et al. 2025; A. King 2025), heavy obscuration by dust-poor or dust-free medium (R. Maiolino et al. 2025; X. Ji et al. 2025a, b), heavy seeds (P. Natarajan et al. 2024), seeding from merging star clusters (C. Partmann et al. 2025; A. Rantala et al. 2025), possibly resulting from 'feedback-free starbursts' (A. Dekel et al. 2025a, b) PopIII and PopIII.1 seeds (J. C. Tan et al. 2024; V. Cammelli et al. 2025; D. Nandal et al. 2025; L. R. Prole et al. 2025; M. Sanati et al. 2025), and primordial BHs (PBHs, P. Dayal 2024; P. Dayal & R. Maiolino 2025; S. Zhang et al. 2025; F. Ziparo, S. Gallerani & A. Ferrara 2025), just to mention a few.

About 10 to 30 per cent (K. N. Hainline et al. 2025) of the newly discovered broad-line AGN have a peculiar V-shaped continuum, with blue ultraviolet (UV) slope and red optical slope. These have been dubbed 'Little Red Dots' (LRDs; D. D. Kocevski et al. 2023; J. Matthee et al. ; R. E. Hviding et al. 2025). They typically show absorption in the Balmer lines (J. Matthee et al. ; I. Juodžbalis et al. 2024a; F. D'Eugenio et al. 2025b, c; X. Lin et al. 2025a), which indicates absorption by large columns of dense gas along the line of sight (K. Inayoshi & R. Maiolino 2025; I. Juodžbalis et al. 2024a; S.-J. Chang et al. 2025), probably associated with absorption that might be responsible for the observed X-ray weakness. They are typically characterized by prominent (though often smooth) Balmer breaks; although these were initially interpreted as originating from evolved stellar populations, it has later been shown that these are connected with the Balmer absorption features and associated with dense gas absorption (K. Inayoshi & R. Maiolino 2025; A. Graaff et al. 2025; R. P. Naidu et al. 2025; F. D'Eugenio et al. 2025b; X. Ji et al. 2025a). LRDs are typically found at $z > 4$ and steeply declining in number density at later cosmic epochs, although luminous examples have been found at $z \sim 2$ (B. Wang et al. 2025; I. Juodžbalis et al. 2024a; Euclid Collaboration 2025; F. Loiacono et al. 2025) and, more recently, a few local counterparts have been identified (X. Ji et al. 2025b; X. Lin et al. 2025b).

One of the first discovered and most prototypical LRD is A2744-QSO1 (hereafter QSO1). This is a strongly lensed, triply imaged LRD, initially identified via imaging with the JWST Near Infrared Camera (NIRCam) in the field of the cluster A2744 (L. J. Furtak et al. 2023) and then spectroscopically confirmed to be at $z = 7.04$ with prism spectroscopy (L. J. Furtak et al. 2024), using the Micro-Shutter Assembly (MSA) of the Near Infrared Spectrograph (NIRSpec). The lensed images are unresolved, with an upper limit on the (continuum) size of only 30 pc in radius. Low-resolution spectroscopy also revealed broad Hβ, typical of type 1 AGN, a prominent Balmer break, and the V-shaped continuum typical of LRDs. Already based on the low-resolution spectrum L. J. Furtak et al. (2024) indicated that this LRD hosts an AGN with a mass of $M_{\rm BH} \sim 3 \times 10^7$ M$_\odot$. Y. Ma et al. (2025) investigated further the spectral shape of the continuum of this object by highlighting the difficulty of reproducing it, especially its Balmer break, with simple stellar or AGN models. Their fiducial model ascribed the break to an evolved stellar population with a mass of 4×10^9 M$_\odot$, which, given the extremely compact size, would imply an extremely high stellar surface density (1.4×10^6 M$_\odot$ pc^{-2}), not seen in any other local or lower redshift galaxies with similar or higher masses. However, X. Ji et al. (2025a) obtained data with the Integralf Field Unit (IFU) of NIRSpec as part of the BlackTHUNDER programme, both with the prism and with the high-resolution grating, revealing Hβ absorption; they showed that both the Balmer break and Hβ absorption can be fully explained in terms of extremely dense gas absorption along the line of sight. They also disentangled the narrow component of Hβ, as well as [O III]5007, which are both spectrally unresolved; from these they obtain a tight upper limit on the dynamical mass of the host galaxy, which turns out to be an order of magnitude lower than the stellar mass inferred when assuming a stellar origin of the Balmer break – this is further confirmation that the Balmer break is non-stellar in origin. Furthermore, both X. Ji et al. (2025a) and L. J. Furtak et al. (2025) also detect variations of the EW(Hβ) of the three images of QSO1, indicative of source variability and, therefore, unambiguously confirming that QSO1 is hosting an accreting BH and also the non-stellar nature of the optical continuum. F. D'Eugenio et al. (2025b) extended the wavelength range of the BlackTHUNDER NIRSpec–IFU data to fully cover Hα, confirming the presence of prominent Balmer absorption and obtaining tighter constraints on the host galaxy's dynamical mass.

More recently, I. Juodžbalis et al. (2025b) performed a more detailed analysis of the BlackTHUNDER data of QSO1, focusing on Hα, to trace the inner rotation curve of the system. They leverage the gravitational lensing sheer, together with independent analyses using spectroastrometry and detailed kinematic modelling (using the Modelling Outflows and Kinematics of Agn in 3D - MOKA3D- environment, C. Marconcini et al. 2023), to resolve the sphere of influence of the BH. Their analysis has revealed a pure Keplerian rotation around a point mass of 5×10^7 M$_\odot$; this direct determination of the BH, is fully consistent with the BH mass estimation inferred from the broad Hβ and using single-epoch virial relations calibrated locally (L. J. Furtak et al. 2024; X. Ji et al. 2025a). Additionally, I. Juodžbalis et al. (2025b) pointed out that the observed Keplerian rotation leaves little room for any stellar component, with an upper limit of $M_{\rm star} < 2 \times 10^7$ M$_\odot$. Their constraint results into a tight lower limit on the BH-to-stellar mass ratio of $M_{\rm BH}/M_{\rm star} > 2$, which is the highest ever found.

Another interesting feature of the original prism spectrum of QSO1 is the faintness of the [O III]5007 line. This, per se, would not necessarily be an anomaly among AGN, and may simply indicate a weak narrow-line region (NLR), which was found in the past for powerful quasars at high redshift (H. Netzer et al. 2004), although much more luminous than QSO1. However, the high-resolution spectrum has shown a clear narrow component of both Hβ and Hα, revealing that an NLR, or ISM (interstellar medium) ionized by star formation, is actually present and that [O III]5007 is actually anomalously weak relative to the narrow components of the hydrogen lines. In this paper, we analyse the BlackTHUNDER high-resolution data to assess the [O III] weakness more thoroughly and more quantitatively, and show that it is tracing very low metallicity of the gas embedding the BH. We also discuss the possible implications for our understanding for BH seeding.

A flat Lambda-cold dark matter cosmology is adopted throughout based on the latest results of the Planck Collaboration VI (2020), with $H_0 = 67.4\,{\rm km\,s^{-1}\,Mpc^{-1}}$, $\Omega_{\rm m} = 0.315$, and $\Omega_{\rm b} = 0.0492$. At $z = 7.04$, an on-sky separation of 1 arcsec corresponds

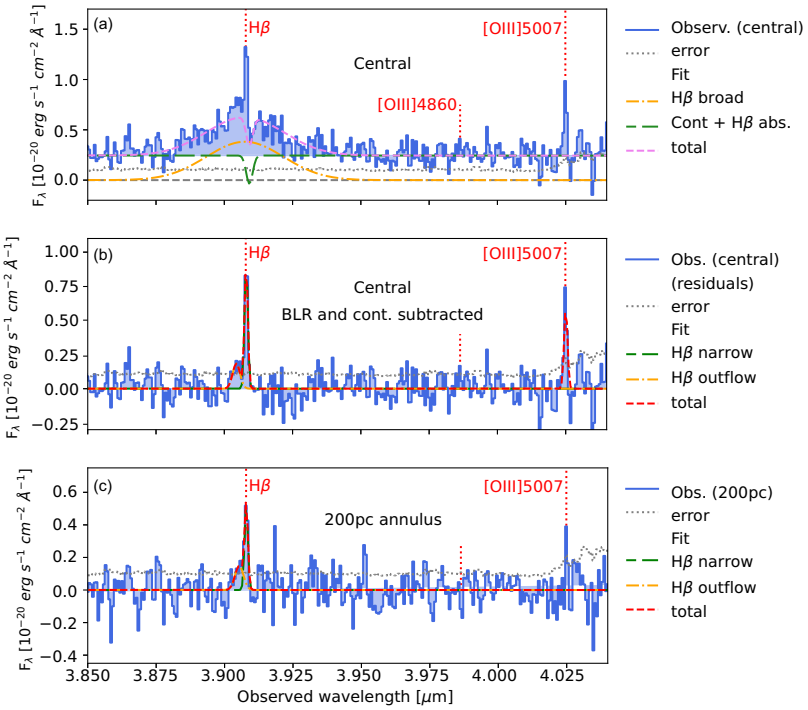

Figure 1. Spectra of QSO1 around Hβ and [O III]5007. (a) Spectrum extracted from the central region (blue solid line), with the fitted broad component of Hβ (orange dot-dashed line), continuum and Hβ absorption (green long-dashed line), as in X. Ji et al. (2025a), while the violet short-dashed line shows the total fit. (b) The same central spectrum where the broad Hβ, continuum and Hβ absorption have been subtracted to highlight the narrow component of Hβ and [O III]5007. (c) Spectrum extracted from a semi-annulus from 0.1 arcsec ($\sim$ 150 pc) to 0.2 arcsec ($\sim$ 300 pc) from the centre – Hβ is clearly detected while [O III]5007 is formally undetected (flux mostly on a single pixel). In all panels, the dotted grey line shows the 1σ error level.

to 5.53 physical kpc (pkpc). The lensing magnification results into a stretching of this scale by a factor of about 3.5 (L. J. Furtak et al. 2024).

2 OBSERVATIONS AND DATA REDUCTION

We used the NIRSpec–IFU spectral cubes from the BlackTHUNDER programme PID-5015 (PIs: H. Übler and R. Maiolino), already presented in X. Ji et al. (2025a) and F. D'Eugenio et al. (2025b). The observations and data processing are extensively discussed in these two papers. Here, we simply recall that the observations targeted image A of QSO1 (lensing magnification factor $\mu \sim 5.8 - 6.15$, depending on the adopted model, L. J. Furtak et al. 2024; X. Ji et al. 2025a) with the NIRSpec IFU mode, both with the high-resolution disperser *G395H* (for a total exposure of 7.4 h) and with the low-resolution prism (for a total of 2 h), although the latter is not used in this paper. We note that image B has slightly higher magnification but located near a bright foreground galaxy in projection, which makes its analysis more difficult, while image C has a significantly lower magnification, hence the choice of selecting image A for the IFU observation. As discussed more extensively in X. Ji et al. (2025a) and F. D'Eugenio et al. (2025b), the data were processed with the *JWST* pipeline, but with additional steps to correct for the $1/f$ noise and for outliers rejection. Before combination, the cubes were resampled to a scale of 0.05 arcsec spaxel^{-1}. As noted by previous studies, the ERROR extension of the NIRSpec IFU cubes underestimates the real error (H. Übler et al. 2023; B. Rodríguez Del Pino et al. 2024); following the same procedure as previous works, the error extension has been rescaled to match the value measured in regions of the cube free of sources.

3 DATA ANALYSIS: SPECTRAL FITTING AND SPATIAL EXTENSION

Fig. 1(a) shows the spectra extracted from the central 0.2 arcsec, i.e. from within the central $r < 150$ pc. The aperture is not perfectly circular in order to account for the shape of the point spread function (PSF). Unfortunately, the PSF of the IFU observations is difficult to determine, as it does not follow exactly the *JWST* theoretical PSF – it also tends to be slightly elongated along the direction of the IFU's slices (F. D'Eugenio et al. 2025a). In the case of QSO1, we leverage the fact that the continuum is unresolved, based on the NIRCam images (L. J. Furtak et al. 2024) and therefore we can take the continuum as a reference to trace the PSF. We find that the continuum between Hβ and [O III] (the spectral region of main interest), is well described by an ellipse with axial ratio 0.8 and major axis PA $= -25°$. The central extraction aperture is shown by the central ellipse in Fig. 2, overlaid on the map of the Hβ narrow component (hereafter Hβ_N). Note that this map was conservatively created by simply collapsing the three spectral channels (continuum-subtracted) around the peak Hβ_N. This implies that the map includes also some contribution from the broad line, but this does not affect our result as the map is not used for quantitative purposes.

As already shown in X. Ji et al. (2025a) and F. D'Eugenio et al. (2025b), the central spectrum confirms the broad Hβ associated with the AGN's BLR, with Hβ absorption (visible at higher significance in Hα; F. D'Eugenio et al. 2025b). However, most importantly, it clearly reveals a narrow component of Hβ and extremely weak [O III]5007 emission. As already mentioned in the introduction, such weak [O III] emission was also noticed by L. J. Furtak et al. (2024) in the low resolution, prism spectrum, but they could not assess the intensity relative to the corresponding narrow component of Hβ, because the

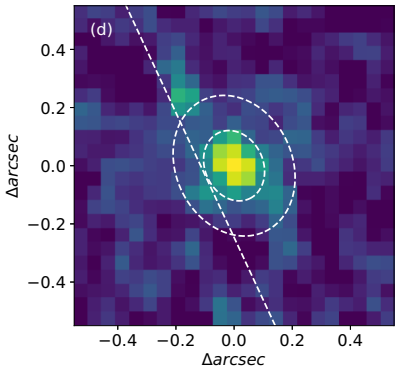

Figure 2. Map of Hβ narrow (obtained by simply collapsing the three central channel of the continuum-subtracted line) with overlaid the central aperture and annulus used for extracting the spectra in panels (a)–(c) of Fig. 1, respectively; [O III] falls in the detector gap in the region on the East (i.e. left) of the dashed straight line, hence this portion of the annulus was not used for extracting the spectrum.

Table 1. Flux ratios for the narrow emission lines.

F([O III]5007)/F(Hβ_N)	(Central)	0.55 ± 0.16
F([O III]5007)/F(Hβ_N)	(R∼200)	< 0.41
F([O III]5007)/F([O II]3727)	(Central)	> 3.1
F([O III]4363)/F([O III]5007)	(Central)	< 0.30
F([S II]6717, 6731)/F(Hα_N)	(Central)	< 0.08
F([N II]6584)/F(Hα_N)*	(Central)	< 0.29
F(Hα_N)/F(Hβ_N)*	(Integrated)	$2.6^{+0.6}_{-0.5}$

Note. * From F. D'Eugenio et al. (2025b).

latter is blended with the broad component coming from the BLR in the prism spectrum. In the new high-resolution spectrum, it is possible to spectrally resolve and disentangle the broad component of Hβ (FWHM $\sim$ 2600 km s^{-1}) from the narrow component (which is spectrally unresolved, with FWHM $<$ 75 km s^{-1}), as illustrated in Fig. 1(a). We adopt the same fitting approach as in X. Ji et al. (2025a), with Gaussian components (with lower limit widths given by the spectral resolution) to disentangle the narrow and broad Hβ components, and which also includes an absorption component, and [O III]5007. We could in principle also include Hα in the simultaneous fitting (as in F. D'Eugenio et al. 2025b), but our focus is on the [O III]/Hβ ratio, while the different PSF at the wavelength of Hα, convolved with the extension of the emission (discussed later), could introduce artefacts – however, re-assuringly we obtain flux ratios that are fully consistent with those obtained by F. D'Eugenio et al. (2025b). The spectrum extracted from the central aperture with radius of 0.1 arcsec, subtracted of the broad component and continuum, is shown in Fig. 1(b), further highlighting the prominence of the narrow component of Hβ (Hβ_N) and the weakness of [O III]5007. Hβ has a residual weak blue wing after subtracting the broad component, which (as discussed further below) is spatially resolved and probably associated with an outflow, which we fit with a separate Gaussian and whose flux is not included in Hβ_N.

The inferred ratio between [O III]5007 and Hβ_N is extremely low, less than unity ([O III]5007/Hβ_N $\sim$ 0.6), as reported in Table 1. It should be noted that the Gaussian fit of [O III]5007 does not capture the full profile of the line; this is because the narrow components are unresolved and poorly sampled by the NIRSpec spectral pixels. Low spectral sampling is also the reason why the peak of [O III] relative to Hβ_N appears somewhat higher than the $\sim$ 0.6 ratio given by the flux

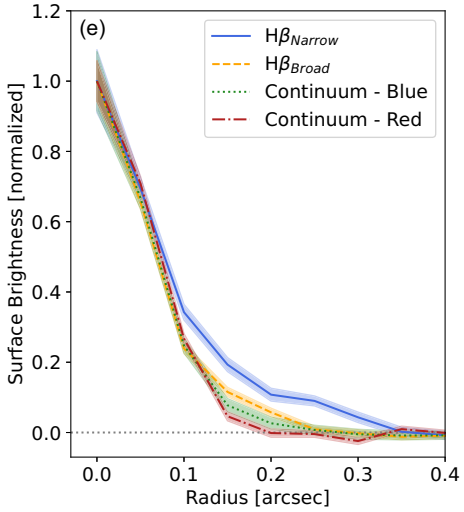

Figure 3. Radial profiles (normalized to the peak) of the narrow component of Hβ (solid blue, the shaded area is 1σ error on the mean), the broad component of Hβ (dashed orange), the continuum on the blue side of Hβ (dotted green), and the continuum on the red side of Hβ (dot–dashed red), which trace the PSF. The narrow component has a compact core, but it also shows a clear extended component.

ratio – when lines are unresolved and poorly sampled, the intensity of the line peaks also depends on how the line flux is distributed on the few spectral pixels. However, we have checked that the simple integration of the flux in the spectral pixels covering the lines give the same flux ratios as the Gaussian fits.

As we will discuss further in Section 4, such extremely low [O III]/Hβ_N ratio is very rarely found among high-z galaxies and generally interpreted in terms of extremely low metallicity.

As also pointed out by I. Juodžbalis et al. (2025b), who presented a spatially resolved analysis of Hα in QSO1, the hydrogen lines have some spatial extension. While I. Juodžbalis et al. (2025b) focused on Hα, here we focus on Hβ as we need it in comparison with [O III]. The Hβ extension is noticeable in Fig. 3, which shows the radial profile of Hβ_N (blue solid line), compared with the radial profile of the broad component of Hβ and the continuum. For simplicity and to avoid degeneracies, the radial profile of Hβ_N shown in Fig. 3 is obtained by simply collapsing the three spectral channels around the peak of Hβ_N; this is conservative as it implies that the actual radial profile of Hβ_N is probably even more extended (as it includes also some contribution from the broad line). As already mentioned, given that the continuum is not resolved in the NIRCam images, it can be used to trace the PSF. The profile of the continuum blueward of Hβ was obtained by collapsing the spectral channels in the region 3.700–3.835 μm (green dashed line), and the profile of the continuum redward of Hβ was obtained by collapsing the spectral channels in the region 3.944–3.700 μm (red dot–dashed line). The profile of broad $H\beta$ (dashed orange line) is extracted from the high S/N region between 3.894–3.904 μm; this also includes part of the 'blue wing', which we tentatively ascribe to a low-metallicity outflow, on the grounds that this profile is slightly more extended than the continuum and also seen in the outer annulus, which is discussed further below. The comparison of the profiles illustrates that, while a large fraction Hβ_N comes from a very compact, unresolved region, it also has a component extending on scales of $\sim$ 0.2 arcsec ($\sim$ 300 pc deprojected). The broad component of Hβ has some indication of extension, likely because it includes the weak blue wing (with smaller

width relative to the broad component) that is probably tracing an outflow.

Motivated by the observed extension of Hβ_N, in Fig. 1(c) we also show the spectrum extracted from a semi-annulus with radius between 0.1 and 0.2 arcsec (150–300 pc) from the centre; note that we had to exclude the south-west part of the annulus because of [O III] falling in the detectors gap in that region (this is the region to the SE of the dashed line in Fig. 2). The contamination from the spectrum in the central region (due to the wings of the central PSF) to the spectrum extracted from the annulus is estimated to be below 15 per cent; this is confirmed by the fact that the the broad Hβ is undetected in the spectrum of the annulus. There is a weak blue wing, which may originate from a mild outflow, as discussed above. Yet, the most important finding is that Hβ_N is still clearly detected. There is only a weak hint of [O III]5007, which is formally undetected (the putative flux is only on one single spectral pixel, much narrower than the line spread function). The inferred upper limit of the narrow-line ratio in this annulus is even lower than in the central region: [O III]/H$\beta_N < 0.41$ (3σ). Note that this is a conservative upper limit – some contamination from the central spectrum (where the [O III]/Hβ_N ratio is higher) to the narrow lines would imply that the upper limit on the [O III]/Hβ_N ratio in the annulus is even lower.

4 EVIDENCE FOR VERY LOW METALLICITY

As already mentioned, the extremely low [O III]/Hβ_N ratio is very rarely found among high-z galaxies (M. Curti et al. 2024; E. Vanzella et al. 2023, 2025; T. Y.-Y. Hsiao et al. 2025; T. Morishita et al. 2025; K. Nakajima et al. 2025) and, in these low-mass systems, is explained in terms of extremely low metallicity (K. Nakajima & R. Maiolino 2022; K. Nakajima et al. 2022). In Appendices C and D, we discuss that, unlike the Hβ broad (from the BLR), alternative scenarios for explaining the low [O III]/Hβ (such as extremely high density of the ISM or low ionization) are physically implausible.

As discussed in F. D'Eugenio et al. (2025b), given the extremely narrow width of [O III], Hβ_N, and Hα_N, these components are likely powered by weak star formation in the host. We therefore infer the metallicity by using the calibrations recently derived for high-z star-forming galaxies. However, in Appendix B, we show that the results would hold, and would actually be reinforced, also assuming photoionization by the AGN. Fig. 4(a) shows the location of QSO1 on the [O III]/Hβ versus metallicity diagram, calibrated by R. L. Sanders et al. (2024, red solid line). For comparison we show (with small blue circles) direct, individual metallicity measurements of high-z galaxies collected by E. Cataldi et al. (2025), while green squares indicate additional high-z galaxies at low metallicity, for which the metallicity has been measured directly (L. Mowla et al. 2024; F. Cullen et al. 2025; C. J. Willott et al. 2025), and the purple pentagons show the median values inferred by the Assembly of Ultradeep Rest-optical Observations Re- vealing Astrophysics (AURORA) survey at high-z (R. L. Sanders et al. 2025). The R. L. Sanders et al. (2024) calibration provides a metallicity 4.7×10^{-3} $Z_\odot$ for the central region, and an upper limit of 3.9×10^{-3} $Z_\odot$ for the ∼200 pc extended region (based on the 3σ upper limit on [O III]/Hβ). There is potentially a highly super-solar solution (high-metallicity branch) that, in addition to being highly implausible for such a small system at such high redshift, is ruled out (shaded region) by the weakness of the low-ionization lines ([O II]3727 and [S II]6720). This is discussed more in detail in Appendix A.

We note that we are adopting an extrapolation of the R. L. Sanders et al. (2024) calibration to low metallicities, just as other studies

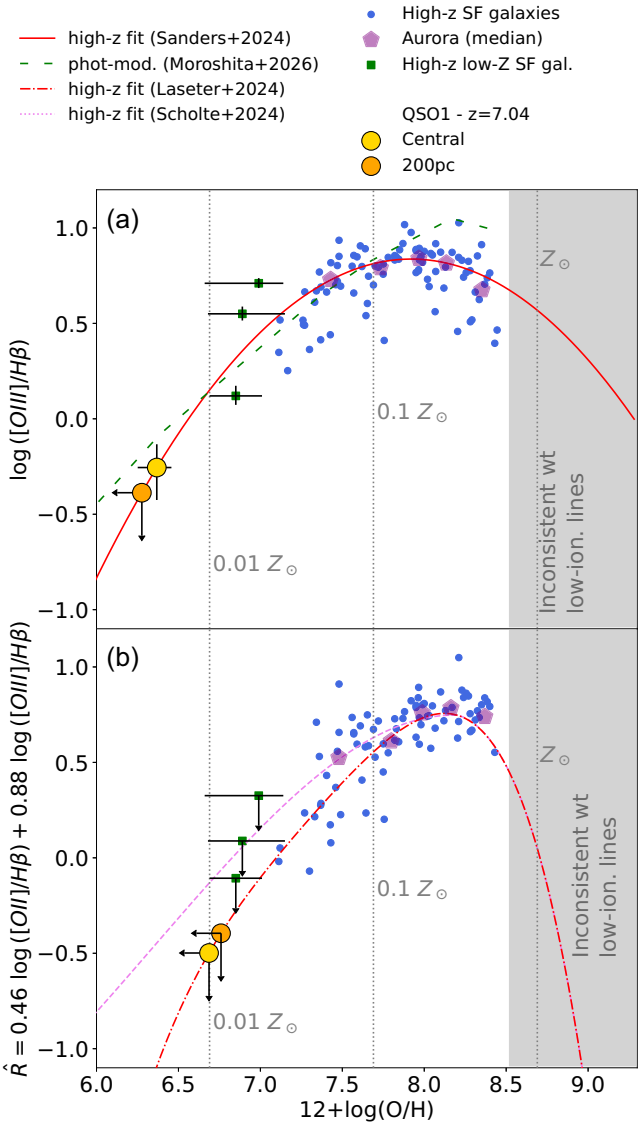

Figure 4. Metallicity constraints on QSO1 inferred from the observed emission-line ratios. (a) [O III]5007/Hβ versus 12 + log(O/H); and (b) $\hat{R} = 0.46\ R_2 + 0.88\ R_3$ versus 12 + log(O/H). The red solid line shows the calibration for [O III]/Hβ from R. L. Sanders et al. (2024) and while the red dot–dashed line shows the calibration for $\hat{R}$ from I. H. Laseter et al. (2024), in both cases using high-z star-forming galaxies. Small blue circles are individual, T_e-based measurements at high-z from E. Cataldi et al. (2025). Green squares are other high-z galaxies at low metallicity (L. Mowla et al. 2024; F. Cullen et al. 2025; C. J. Willott et al. 2025). Purple pentagons are median values at high redshift from the AURORA survey (R. L. Sanders et al. 2025). The QSO1 line ratios are shown with large circles, yellow and orange for the central region and for the annulus at ∼200 pc, respectively. The green long-dashed line in (a) is the photoionization models relation by K. Nakajima & R. Maiolino (2022) adopted by T. Morishita et al. (2025) and short-dashed purple line in (b) is the calibration for $\hat{R}$ from D. Scholte et al. (2025); both these alternative calibrations would give even lower metallicities. The shaded area indicate the high-metallicity solutions excluded by the low-ionization lines (Methods). In both panels, error bars are at 1σ, while upper limits are at 3σ.

Table 2. Physical properties inferred for QSO1.

$\log(Z/Z_\odot) = -2.32^{+0.09}_{-0.12}$ $[R < 150$ pc$]$
$\log(Z/Z_\odot) < -2.41$ $[150$ pc $< R < 300$ pc$]$
[a] $A_V < 0.5$
[b] $\log(M_{\rm BH}/M_\odot) = 7.7 \pm 0.3$
[b] $L/L_{\rm Edd} \approx 0.03$
[b] $M_{\rm star} < 2 \times 10^7$ $M_\odot$
[b] $M_{\rm BH}/M_{\rm star} > 2$

Notes. [a] From F. D'Eugenio et al. (2025b); and [b] from I. Juodžbalis et al. (2025b).

of other similar extremely low-metallicity systems. However, unlike other works (T. Morishita et al. 2025; K. Nakajima et al. 2025), the calibration adopted by us is more conservative. Indeed, other calibrations used by other works, would give even lower metallicities. As an example, the photoniozation models by K. Nakajima & R. Maiolino (2022) with the highest ionization parameter ($\log(U) = -0.5$, green long dashed line in Fig. 4a), used by K. Nakajima et al. (2025) and T. Morishita et al. (2025) in their low-metallicity galaxies at high-z, would give an even lower metallicity, by 0.2–0.3 dex.

Fig. 4(b) shows also the calibration using the parameter $\hat{R} = 0.46\ \log([\mathrm{O\,II}]/\mathrm{H}\beta) + 0.88\ \log([\mathrm{O\,III}]/\mathrm{H}\beta)$, initially proposed by I. H. Laseter et al. (2024), which has the advantage of being more steeply declining at low metallicities. In this case, we only have upper limits on this parameter (as [O II]3727 is not detected), but which give upper limits on the metallicity ($Z < 10^{-2}\ Z_\odot$) consistent with the values in Fig. 4(a). Also in this case we are using a conservative calibration obtained at high redshift – using the alternative calibration by D. Scholte et al. (2025, red dashed line in Fig. 4b) would give upper limits that are 0.3–0.4 dex lower.

The inferred constraints on the metallicity are summarized in Table 2, together with other relevant properties for QSO1.

5 DUST EXTINCTION

The ratio between the narrow components of Hα and Hβ has been measured by F. D'Eugenio et al. (2025b) to be $2.6^{+0.6}_{-0.5}$, i.e. consistent with Case B, hence indicating no or negligible dust extinction ($A_V < 0.5$). This is fully consistent with our finding of extremely low metallicity, which is expected to be accompanied by little dust.

Within the context of this section it is worth mentioning that a very low metallicity is also independently derived by F. D'Eugenio et al. (2025b), from the properties of the absorbing gas, who infer a very low dust content, specifically $Z\xi_d < 3 \times 10^{-4}$, where ξ_d is the dust-to-metal ratio. Assuming an evolution of ξ_d as a function of Z as obtained by C. Konstantopoulou et al. (2024), this would imply $Z < 4 \times 10^{-3}\ Z_\odot$, consistent with the upper limit that we have inferred in the outer region of QSO1 from the [O III]/β ratio.

6 OUTFLOW AND BLACK HOLE MASS

We will see that our inferred metallicity measurement already provides important constraints on models and simulations. However, these constraints become even more stringent if accompanied by constraints on the BH mass. Therefore, in this section, we provide a brief overview of the BH mass measurement presented for QSO1 and also take the opportunity to discuss more the profile of the broad component of the Balmer lines, although an in depth discussion of these aspects is beyond the scope of this paper.

The BH mass in QSO1 was first estimated by L. J. Furtak et al. (2024) to be $\log(M_{\rm BH}/M_\odot) \approx 7.5$ based on the profile of Hβ in their low-resolution prism spectrum and assuming the local virial relations (A. E. Reines & M. Volonteri 2016). These relations allow the BH mass to be inferred based on the broad Balmer emission lines' luminosity and their width or dispersion. However, in their low-resolution spectrum, the broad component of Hβ was marginally resolved and totally blended with the narrow component.

X. Ji et al. (2025a) derived a BH mass in the range $\log(M_{\rm BH}/M_\odot) = 7.2 - 7.6$, depending on the assumed extinction and methodology, and based on the broad component of Hβ measured in their high-resolution spectrum, fitted with a single broad Gaussian.

As we discussed, fitting the broad Hβ with a single Gaussian gives the residual of an intermediate component, slightly blueshifted relative to the narrow component. The fact that this component is spatially resolved on scales of a few 100 pc strongly suggests that this component is tracing an outflow. I. Juodžbalis et al. (2025b) investigated the higher S/N and higher resolution spectrum of Hα; they also identify the intermediate component of Hα and they also find that it is extended on scales of a few 100 pc (although the angular resolution at the wavelength of Hα is 50 per cent lower than at the wavelength of Hβ).

This intermediate component is not seen in [O III], but it would not be detectable if it had the same ratio to Hβ as the narrow components. This suggests that also the outflow is very metal poor. This is a very fascinating aspect, as it may highlight early feedback processes in these primeval BHs. However, a more extensive analysis of the outflow in this source is beyond the scope of the paper and will be presented in a separate work. Here, we only mention that if this intermediate component was included in the computation of the BH mass it would have reduced it, as the effective width of the combined broad line would have been smaller.

By taking only the spatially unresolved, broader component of Hα (i.e. the one most likely associated with the BLR), and correcting for the mild extinction inferred from the narrow Balmer decrement, F. D'Eugenio et al. (2025b) estimate a BH mass of $\log(M_{\rm BH}/M_\odot) = 7.1 \pm 0.3$, i.e. consistent with the estimate from Hβ.

All these estimates are based on single epoch measurements, relying on virial relations that are calibrated locally, either through reverberation mapping or direct measurements (e.g. A. E. Reines & M. Volonteri 2016; E. Dalla Bontà et al. 2025). There has recently been much debate about whether such relations are adequate at high redshift especially for LRDs, with works claiming that such relations may overestimate the BH masses by two orders of magnitude (S.-J. Chang et al. 2025; R. P. Naidu et al. 2025; V. Rusakov et al. 2025), while others claiming that the BH masses might be underestimated by large factors when accreting close or beyond the Eddington limit (A. Marconi et al. 2008, 2009). The direct BH mass determination of a luminous quasar at $z = 2.3$, through the spatially resolved observation of its BLR with interferometry, has found a value consistent with the virial relations within a factor of 2.5, when using Hα. However, LRDs, and more generally AGN at even higher redshifts, may behave differently.

Yet, specifically for QSO1, I. Juodžbalis et al. (2025b) used the BlackTHUNDER data to resolve the rotation curve traced by the narrow lines in the inner region, down to the central few tens pc, also thanks to the gravitational magnification. They leverage both spectro-astrometry and detailed dynamical modelling using the MOKA3D framework (C. Marconcini et al. 2023), which reproduces both the velocity field and the light distribution by taking into account also the PSF smearing. They find that the kinematics is consistent with pure Keplerian rotation around a point mass of $\log(M_{\rm BH}/M_\odot) = 7.7 \pm 0.3$. This is consistent within the uncertainties, with the BH masses estimated via virial relations.

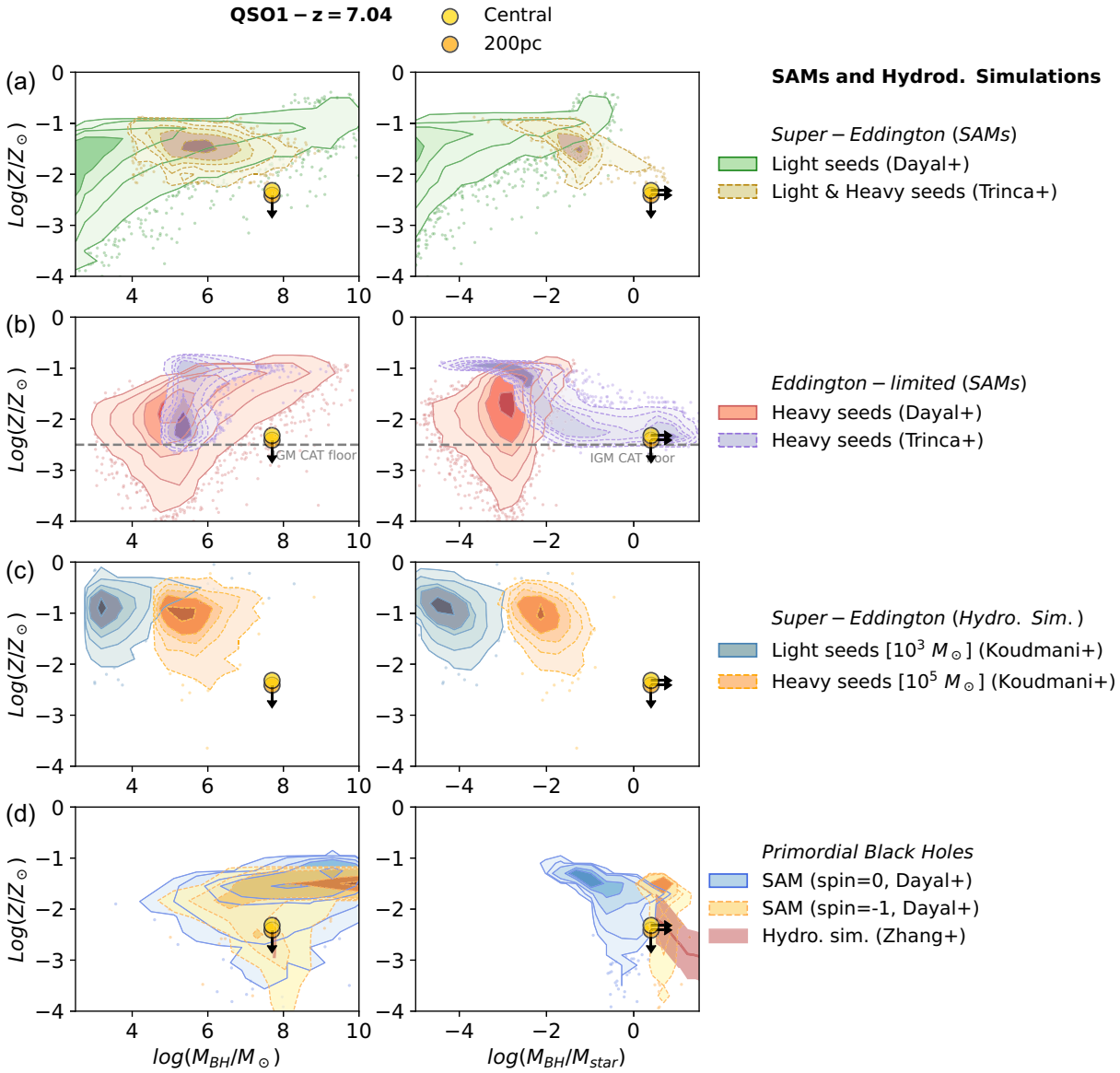

Figure 5. Comparison of the QSO1 properties with SAMs and hydrodynamical simulations on the metallicity versus $M_{\rm BH}$ (left) and metallicity versus $M_{\rm BH}/M_{\rm star}$ (right) diagrams. Description of all models are provided in the text and in Appendix G. Contours enclose 1 per cent, 30 per cent, 68 per cent, 84 per cent, 95 per cent, and 99 per cent of the models or simulations. Models and simulations outside the 99 per cent countours are plotted individually. For the PBH hydrodynamical simulations, the red thick line shows the evolution of a representative case, and the shaded regions indicate the uncertainty on the metallicity. The golden (uppper) and orange (lower) circles show the properties of QSO1 in the central aperture and in the outer annulus ($\sim$ 200 pc from the centre), respectively (upper limits are at 3σ).

As already mentioned in the Introduction, I. Juodžbalis et al. (2025b) also noted that the Keplerian curve leaves little room for any stellar component in the host galaxy, yielding a tight dynamical upper limit on the stellar mass of 2×10^7 M$_\odot$. This results into an unprecedented lower limit on the BH-to-stellar mass ratio of $M_{\rm BH}/M_{\rm star} > 2$.

The upper limit on the stellar mass given above is assuming an exponential stellar disc (Sérsic index $= 1$); the upper limit becomes even lower if one considers the scenario of a very compact nuclear star cluster (see I. Juodžbalis et al. 2025b).

In the rest of this paper, we will adopt the direct measurement of the BH mass obtained by I. Juodžbalis et al. (2025b) and, conservatively, the BH-to-stellar mass lower limit inferred by them when assuming an exponential disc.

7 COMPARISON WITH MODELS AND SIMULATIONS

In most scenarios of BH–galaxy co-evolution it is difficult to grow a BH with masses in excess of 10^7 M$_\odot$ while keeping the metallicity of the ISM as low as 10^{-2} $Z_\odot$. Therefore, the findings presented in this paper are indicative of some specific route that allowed the BH to form and grow in a very un-evolved stellar system.

In this section, we compare our results with predictions of various models and simulations, which are described more in detail in Appendix G, and which are not meant to be exhaustive.

Fig. 5 shows the location of QSO1 on the metallicity versus BH mass plane, and versus BH-to-stellar mass ratio. The large symbols show the locations of QSO1 as inferred by our analysis (Table

2), both considering the metallicity measured centrally (golden) and in the 200 pc annulus (orange), together with the BH mass measurement and BH-to-stellar mass ratio constraint directly inferred by I. Juodžbalis et al. (2025b), as discussed more in detail in Section 6. In terms of M_{BH}/M_{star} ratio, it is not totally obvious whether we should take the total upper limit on M_{star} or values estimated matching the extraction apertures. Different models and simulations generally provide integrated values and generally do not resolve these small scales; additionally, as discussed, the upper limit on the stellar mass depends on the assumed profile (exponential disc vs. nuclear star cluster). For the sake of simplicity, we take the global upper limit inferred by I. Juodžbalis et al. (2025b) on the stellar mass assuming an exponential profile. We recall that this upper limit was obtained by modelling the rotation curve traced by the narrow Hα, which gave an upper limit on the dynamical mass of the host galaxy of $M_{dyn} < 2 \times 10^7$ M$_\odot$, and therefore a tight upper limit on the stellar mass. This gives a tight lower limit on the BH-to-stellar mass ratio of $M_{BH}/M_{star} > 2$, that, for simplicity, we associate to both the central region and the 200 pc annulus, making it clear that this is a conservative lower limit.

In Fig. 5(a), the contours show the distribution of semi-analytical models (SAMs) at $z = 7$ which assume SE accretion. In all plots, the outermost contour includes 99 per cent of the distribution. Green solid contours are for models from the DELPHI (Dark matter and the Emergence of gaLaxies in the ePocH of reIonization) SAMs (P. Dayal et al. 2025) with light seeds (100 M$_\odot$) that are allowed to accrete at up to five times higher than the Eddington limit. The dashed brown contours are from the SAM CAT (COSMIC ARCHAEOLOGY TOOL) models (A. Trinca et al. 2024a) involving both light and heavy seeds ($10^2 - 10^5$ M$_\odot$), allowed to accrete up to tens of times above Eddington for short phases. These SAM models struggle to reproduce the observations. However, a small fraction of the CAT SAMs can potentially be marginally consistent with the properties of QSO1, altough in less than 1 per cent of the cases. This tail is part of the models that started with heavy seeds.

One should however consider that, as we discuss in the next section, QSO1 is not a rare object at $z > 7$ – it is probably fairly common among AGN at $z > 7$. Therefore, successful models and simulations should also reproduce a relatively large fraction of these objects. On the other hand, these SAMs (as well as simulations discussed further below) were optimized to reproduce populations of BHs that did not include cases like QSO1. Probably, future optimization in the assumptions of these SAMs will be more successful in reproducing the observational properties of QSO1.

Fig. 5(b) shows the DELPHI and CAT models at $z = 7$ in the scenario of heavy seeds ($10^3 - 10^5$ M$_\odot$) whose accretion is Eddington limited. These scenarios can reach lower metallicity at $z \sim 7$ relative to the SE model. The primary reason is that in the SE models the excess of gas inflow required to boost BH accretion also results in boosting star formation that rapidly enriches the ISM. One should note that the CAT SAMs have a metallicity floor that is given by the modelling assumption that the IGM (intergalactic medium) metallicity at this epoch is $\log(Z_{IGM}/Z_\odot) = -2.5$ (horizontal dashed line). Both these Eddington-limited (EL) models fail to either achieve the required BH mass, or the required M_{BH}/M_{star} ratio at the observed metallicity. Essentially these models do not manage to grow the BH large enough, unless they are accompanied by significant star formation in the host, which both significantly increases the metallicity and significantly reduces the BH-to-stellar mass ratio.

Fig. 5(c) illustrates the case of the AESOPICA hydrodynamical simulations based on the FABLE model (N. A. Henden et al. 2018) with modifications to the BH modelling (S. Koudmani, D. Sijacki & M. C. Smith 2022) to allow for very high accretion rates up to 10 times the Eddington limit. Orange dashed contours show the case of heavy seeds (10^5 M$_\odot$), while grey solid contours show the case of the upper boundary for light seeds (10^3 M$_\odot$). In these hydrodynamical simulations light seeds, even accreting at SE rates, are completely excluded. The case of heavy seeds also struggles to reproduce QSO1 because of its low metallicity, but also because of the high M_{BH} and high M_{BH}/M_{star}. However, as already discussed, one should take into account that these simulations, as well as the SAMs discussed above, are developed with assumptions aimed at reproducing BHs with properties quite different than QSO1. Future upgrades may provide a better match with QSO1. For instance, heavier seeds, with masses up to $\sim 10^6$ M$_\odot$ (still consistent with, for instance, the Direct Collapse scenario), may result in a distribution closer to QSO1. Additional gas inflows, kept warm by the UV radiation and prevented from forming additional stars, could help to significantly dilute the metallicity to the level observed in QSO1.

Fig. 5(d) shows the case of 'PBHs', i.e. BHs that, according to some scenarios, might have formed in the ultra-early universe, in the first second after the big bang, possibly reaching back to the inflationary era (e.g. S. Hawking 1971; B. J. Carr & S. W. Hawking 1974; K. M. Belotsky et al. 2019; A. Escrivà, F. Kühnel & Y. Tada 2024; A. Riotto & J. Silk 2024; B. Zhang, W.-X. Feng & H. An 2025). Although the relevance of PBHs as dominant dark matter candidates has been mostly ruled out (e.g. F. Ziparo et al. 2022; C. Casanueva-Villarreal et al. 2025), they are still considered viable as seeds for the subsequent growth of massive BHs. In this scenario, BHs would be the very first structures formed in the Universe, much earlier than stars and galaxies. The expected mass function of PBHs is very uncertain, also because they are expected to be very clustered (K. M. Belotsky et al. 2019; B. Zhang et al. 2025), possibly causing them to rapidly merge hierarchically and, therefore, shift their distribution towards higher masses soon after the big bang. The blue, solid contours in Fig. 5(d) show a version of the PHANES (Primordial black Holes Accelerating the assembly of Nascent Early Structures) analytic model (P. Dayal 2024; P. Dayal & R. Maiolino 2025) in which the growth of haloes and their baryonic components is seeded by PBHs, and in the subcase of non-spinning BHs (Appendix G1). This model can reproduce QSO1 within a few per cent of the distribution, i.e. reasonably well considering the uncertainties associated with this class of BHs. The case of counter-rotating PBHs (spin $= -1$) in the same model is shown with orange, dashed contours; considering that we have only a lower limit on $M_{BH}/M_{star} > 2$, these models can potentially reproduce QSO1 even better. However, one should consider that counter-rotation can be maintained by the BH only for a few Eddington times.

The red thick track in Fig. 5(d) shows the result of hydrodynamical simulations (S. Zhang et al. 2025), which follow the evolution of PBHs, assuming the case of a 5×10^7 M$_\odot$ PBH. This mass is higher than the canonical 10^6 M$_\odot$ scale preferred for PBHs, given by the fundamental-physics connection to the electron–positron annihilation epoch in the ultra-early universe (e.g. B. Carr & F. Kühnel 2020); however, as mentioned, PBHs are expected to be highly clustered and may rapidly merge resulting in much heavier seeds (e.g. S. Zhang, V. Bromm & B. Liu 2024). The track in Fig. 5(d) represents snapshots between $7 < z < 9.5$. As discussed in Appendix G5, the metallicity in these simulations is determined at the post-processing stage (which is a limitation that will be tackled in a follow-up study). As illustrated, in these hydrodynamical simulations the assumed BH mass increases very little in this short epoch, whereas the metallicity and M_{star} evolve rapidly with time. Overall, these hydrodynamical simulations incorporating PBHs can

also potentially explain the properties of QSO1, although subject to the specific assumptions underlying the metallicity evolution and the assumed initial mass of the PBH.

Summarizing, the fact that heavy seeds or SE models/simulations reproduce the properties of QSO1 only in rare cases (or fail completely), may highlight some potential problems in these scenarios. As mentioned, it may indicate that these models require additional, major pristine gas inflows to dilute the metallicity. Additionally, stronger feedback processes may be at work, both ejecting metals more efficiently and/or suppressing star formation (and hence the production of metals) more effectively. Alternatively, the underlying BH seeding and growth assumptions may not be adequate to reproduce this population of objects in the early Universe. Heavier seeds, or seeding at later times may be needed.

We re-iterate that those SAMs and simulations were not optimized to reproduce the properties found at $z = 7$ in QSO1. Indeed, for instance, some of these models manage to reproduce the properties of the much more luminous quasars at $z \sim 6$–7 (J. S. Bennett et al. 2024) – although the metallicity of the host galaxies in distant quasars has not been studied in detail yet, based on their spectral properties they are inferred to have metallicities close to solar (e.g. Y. Juarez et al. 2009; S. Wang et al. 2022), and, while they are overmassive in terms of BH-to-stellar mass ratio (M. A. Stone et al. 2024; M. A. Marshall et al. 2025), they are not as extreme as QSO1. On the contrary, reproducing the extremely low metallicity and the very high BH-to-stellar mass ratio in QSO1, and possibly in other AGN at similar redshifts (see the next section), will probably require additional development of those models. Within this context, it is interesting that J. Jeon et al. (2025a) has more recently developed a SAM more specifically tailored to LRDs and also specifically investigating objects like QSO1. While their light seeds scenario (including super-Eddigton accretion) does not manage to reproduce QSO1, their DCBH (Direct Collapse Black Hole) prescription can reproduce the properties of QSO1 reasonably well; however, their BH mass function is nearly 2 dex below recent observations at high redshift (S. Geris et al. 2025). Another problem of the DCBH scenarios is that most of them require a nearby source of UV radiation for photodissociating H_2, while QSO1 is fairly isolated without strong sources of UV radiation in the vicinity, or post-starburst galaxies that may have produced UV radiation in the past. An additional problem of DCBH models specifically for QSO1, as pointed out by I. Juodžbalis et al. (2025b), is that their early growth is limited by the baryon fraction in an atomically cooling halo (V. Bromm & N. Yoshida 2011; F. Pacucci et al. 2015); this sets an upper limit to the BH-to-dynamical mass ratio of ~ 0.1, which is more than 1 dex lower than observed in QSO1, as already discussed earlier on (I. Juodžbalis et al. 2025b).

On the other hand, the fact that scenarios invoking PBHs can explain reasonably well the properties of QSO1-like system, including their seemingly high space density discussed in the next section, indicates that the physics behind this model may possibly account for a significant population of early BHs. As already discussed, the large mass in QSO1 might be problematic to achieve with pure PBHs without invoking significant accretion, which may have also resulted in star formation and chemical enrichment; however, rapid merging of PBHs (which are highly clustered) can potentially increase their mass by a large factor without resulting in star formation and chemical enrichment.

An intermediate scenario which could potentially account for the properties of QSO1 is that of the 'Not Quite Primordial Black Holes' (NQPBHs; W. Qin et al. 2025). These are putative massive seeds formed at $z > 200$, resulting from the direct collapse of clouds, as a consequence of the cosmic microwave background at that redshift being energetic enough to photodissociate H_2. This scenario may help to achieve a higher mass, but even in this case accretion or merging may be required to attain the BH mass of QSO1 for a significant fraction of the objects, as discussed in the next section. More generally, this scenario requires further investigation to explore and predict more quantitatively whether the properties of QSO1 can be reproduced or not.

Yet another intriguing possibility is that QSO1 could be a BH ejected from a nucleus where there were three BHs that interacted and ejected the least massive one. Since this scenario was initially conceived by W. C. Saslaw, M. J. Valtonen & S. J. Aarseth (1974), several groups have further developed this idea and predicting that this population might be relatively abundant (e.g. M. Volonteri, F. Haardt & P. Madau 2003). However, it is not clear how much gas from the parent galaxy may remain bound to the ejected BH, or how much gas may accrete from the IGM. Leaving aside these aspects, it is unlikely that a relatively powerful AGN aligned with the lensing cluster is one of this special cases of ejected BHs. However, certainly this scenario deserves further exploration, both theoretically and observationally.

Finally, we caution that all these comparisons with models are done assuming that, at a given BH mass, the accretion rate is not dependent on metallicity. Additionally, we have been comparing our results for an accreting AGN (although at a fairly low rate of $L_{\rm Edd} \sim 0.03$, according to I. Juodžbalis et al. 2025b) with models and simulations of the whole population of BHs – AGN duty cycles certainly play a role in their detectability, which should be taken into account in future studies.

Regardless of the specific model and simulation, the finding that QSO1 is embedded in such an extremely low-metallicity gas, and that it is nearly 'naked', with little (if any) stellar mass around it ($M_{\rm BH}/M_{\rm star} > 2$), suggests that it is a massive seed in the earliest phase of accretion.

8 HOW COMMON ARE EXTREMELY METAL-POOR AGN AND LRDS IN THE EARLY UNIVERSE?

It is too early to quantitatively assess the fraction and density of extremely metal-poor AGN, and in particular LRDs, in the early Universe, and certainly more observations and statistics are needed. However, we note that QSO1-like BHs cannot be so uncommon. Indeed, QSO1 is one of the two BHs found at $z>7$ in the whole Ultradeep NIRSpec and NIRCam Observations before the Epoch of Reionization (UNCOVER) survey (J. E. Greene et al. 2024), and the only one with $M_{\rm BH} < 10^8$ $M_\odot$. Additionally, it is found in a very small sky area close to the caustic behind the A2744 field (within ~ 30 arcsec) that could produce multiple images, meaning that the volume density of these type of objects cannot be low.

Although the number and quality of observations of low luminosity AGN with intermediate BH masses at $z>7$ are still inadequate to draw conclusions, it is important to compare QSO1 with the few other AGN discovered at $z>7$. Aside from QSO1, there are six type 1 AGN found at $z>7$ (V. Kokorev et al. 2023; J. E. Greene et al. 2024; R. Tripodi et al. 2024; H. Übler et al. 2024; R. Maiolino et al. 2024a; R. P. Naidu et al. 2025; A. J. Taylor et al. 2025b). One of them has an estimated very low metallicity of $Z < 0.1\ Z_\odot$ (R. Tripodi et al. 2024) and two more have very weak [O III]5007 (although their [O III]/Hβ_N is difficult to constrain due to low spectral resolution, R. P. Naidu et al. 2025; A. J. Taylor et al. 2025b), so these might share similar properties as QSO1. Therefore, although statistics are still low, about

half of the AGN discovered by *JWST* at $z>7$ seem to have very low metallicities, possibly as extreme as QSO1.

Summarizing, it is very unlikely that QSO1 is an outlier, and implausible that it is in the tail of a distribution with probability to be found of less than a few per cent. QSO1-like systems must be fairly common among intermediate-mass BHs ($M_{\rm BH}$ a few times 10^7 $M_\odot$) at $z>7$.

However, at the same time, one should also note that the other three AGN at $z>7$ have [O III]/Hβ significantly higher than in QSO1, and likely have higher metallicity. Therefore, the origin of these other BHs may well be different from the one in QSO1. Most of them also have masses much higher than QSO1 and may have formed and grown through different channels (e.g. J. Jeon et al. 2025b). These three AGN at $z>7$ with high [O III]/Hβ would certainly be easier to reproduce by some of the models presented in the previous section, not only because of the probably higher metallicity, but also because they do not have BH-to-stellar mass ratio as high as QSO1.

9 CONCLUSIONS

We have analysed the deep, high-resolution NIRSpec–IFU spectroscopy of A2744-QSO1, obtained as part of the BlackTHUNDER *JWST* Large Programme. QSO1 is a strongly lensed LRD at $z=7.04$, hosting a massive BH ($M_{\rm BH}\approx 5\times10^7$ $M_\odot$, measured directly), and with $M_{\rm BH}/M_{\rm star}>2$. We have focused on the narrow components of the emission lines and, in particular Hβ and [O III]. The high-resolution spectroscopy of the new data allows the clear disentangling of the narrow and broad components of Hβ. Additionally, the high sensitivity of the data, together with the integral field mode and the strong lensing shear, allow the spatial extent of Hβ to be traced. The main results of our analysis are the following:

(i) While the continuum is spatially unresolved, the narrow component of Hβ is spatially extended out to $\sim$ 400 pc.

(ii) In the central region ($R<150$ pc) the [O III]5007 line is extremely weak relative to the narrow component of Hβ, with a ratio [O III]5007/H$\beta=0.66$, one of the lowest ever observed in the ISM of distant galaxies. In an annulus with 150 pc $<R<$ 300 pc Hβ narrow is still clearly detected while [O III]5007 is not significantly detected, resulting [O III]5007/H$\beta<0.41$.

(iii) As in other similar galaxies at high-z, the simplest interpretation of the low [O III]5007/Hβ ratio is very low metallicity of the gas in the vicinity of the BH (while we show that density or ionization effects cannot play a significant role). We estimate $Z\approx4.7\times10^{-3}$ $Z_\odot$ in the central region ($R<150$ pc), and $Z<3.9\times10^{-3}$ $Z_\odot$ in the annulus at about 200 pc.

(iv) We have discussed that massive BHs with such low metallicity are probably fairly common in the early universe, although more data are needed to properly assess their occurrence.

(v) It is challenging for most models to account for such a chemically unevolved system that host a BH that is already so massive. More specifically, we have shown that most models and simulations struggle to reproduce the properties of QSO1, although some of them can reproduce the observed low metallicity, together with the high $M_{\rm BH}$ and high $M_{\rm BH}/M_{\rm star}$. This may indicate that some revision in the assumptions of these models may be required (e.g. additional pristine inflow diluting the metallicity, more massive seeds, or stronger feedback). PBH scenarios seem to better reproduce the properties of QSO1, but even these scenarios require further developments to self-consistently explore the BH and metallicity evolution. The scenarios of NQPBHs, or a BH ejected from the interaction with two other merging BHs, should also be explored more thoroughly.

More qualitatively, the finding of extremely low metallicity, together with the high $M_{\rm BH}$ and extremely high $M_{\rm BH}/M_{\rm star}$, indicates that this LRD, and probably many others at similar redshifts, are tracing the earliest accretion phase on massive BHs seeds (K. Inayoshi 2025). There is clearly the need of additional efforts in modelling and simulating the various BH scenarios in order to properly, and self-consistently reproduce the properties of QSO1 and similar LRDs and AGN in the early Universe.

While we have discussed that other AGN at high redshift seem to be characterized a very low metallicity similar to that observed in QSO1, these other cases need additional observations to be confirmed. Yet, other AGN discovered by *JWST* at $z>7$ are characterized by much higher metallicity relative to QSO1, and these may have formed from different seeds and evolved through different routes relative to QSO1.

ACKNOWLEDGEMENTS

This paper is dedicated to Avishai Dekel, an innovative and inspirational thinker, who made seminal contributions to astrophysics. We thank the anonymous referee for their comments that helped to improve the manuscript. We thank Andrea Ferrara for useful suggestions. This work is based on observations made with the National Aeronautics and Space Administration (NASA)/European Space Agency (ESA)/Canadian Space Agency (CSA) *JWST*. The data were obtained from the Mikulski Archive for Space Telescopes at the STScI, which is operated by the Association of Universities for Research in Astronomy, Inc., under NASA contract NAS 5–03127 for *JWST*. These observations are associated with programme PID 5015. RM, FD, JS, IJ, and GJ acknowledge support from the Science and Technology Facilities Council (STFC), by the European Research Council (ERC) through advanced grant 695671 'QUENCH', by the UK Research and Innovation (UKRI) Frontier Research grant RISEandFALL. RM also acknowledges support from a Royal Society Research Professorship grant. SZ, VB, and BL acknowledge the Texas Advanced Computing Center (TACC) for providing HPC resources under allocation AST23026. GV acknowledges support by European Union's HE ERC Starting grant no. 101040227 – WINGS. HÜ acknowledges funding by the European Union (ERC APEX, 101164796). Views and opinions expressed are however those of the authors only and do not necessarily reflect those of the European Union or the European Research Council Executive Agency. Neither the European Union nor the granting authority can be held responsible for them. KI acknowledges support from the National Natural Science Foundation of China (12233001), the National Key R&D Program of China (2022YFF0503401), and the China Manned Space Program (CMS-CSST-2025-A09).

DATA AVAILABILITY

The NIRSpec data used in this study are publicly available at the STScI MAST archive: https://mast.stsci.edu/portal/Mashup/Clients/Mast/Portal.html, under GO programme 5015, observation 22.

REFERENCES

Ananna T. T., Bogdán Á., Kovács O. E., Natarajan P., Hickox R. C., 2024, ApJ, 969, L18
Baldwin J. A., Phillips M. M., Terlevich R., 1981, PASP, 93, 5
Begelman M. C., Volonteri M., Rees M. J., 2006, MNRAS, 370, 289

Belotsky K. M. et al., 2019, Eur. Phys. J. C, 79, 246
Bennett J. S., Sijacki D., Costa T., Laporte N., Witten C., 2024, MNRAS, 527, 1033
Bondi H., 1952, MNRAS, 112, 195
Bower R. G., Schaye J., Frenk C. S., Theuns T., Schaller M., Crain R. A., McAlpine S., 2017, MNRAS, 465, 32
Bromm V., Loeb A., 2003, ApJ, 596, 34
Bromm V., Yoshida N., 2011, ARA&A, 49, 373
Cameron A. J., Katz H., Witten C., Saxena A., Laporte N., Bunker A. J., 2024, MNRAS, 534, 523
Cammelli V., Monaco P., Tan J. C., Singh J., Fontanot F., De Lucia G., Hirschmann M., Xie L., 2025, MNRAS, 536, 851
Carr B. J., Hawking S. W., 1974, MNRAS, 168, 399
Carr B., Clesse S., García-Bellido J., Kühnel F., 2021, Phys. Dark Universe, 31, 100755
Carr B., Kühnel F., 2020, Annu. Rev. Nucl. Part. Sci., 70, 355
Carr B., Silk J., 2018, MNRAS, 478, 3756
Casanueva-Villarreal C., Padilla N., Tissera P. B., Liu B., Bromm V., 2025, A&A, 699, A49
Cataldi E. et al., 2025, A&A, 703, A208
Chang S.-J., Gronke M., Matthee J., Mason C., 2025, preprint (arXiv:2508.08768)
Chen C.-H., Ho L. C., Li R., Zhuang M.-Y., 2025, ApJ, 983, 60
Chisholm J. et al., 2024, MNRAS, 534, 2633
Costa G., et al., 2025, A&A, 694, A193
Cullen F. et al., 2025, MNRAS, 540, 2176
Curti M. et al., 2024, A&A, 684, A75
Curti M., Mannucci F., Cresci G., Maiolino R., 2020, MNRAS, 491, 944
D'Eugenio F. et al., 2025a, ApJS, 277, 4
D'Eugenio F. et al., 2025b, preprint (arXiv:2503.11752)
D'Eugenio F. et al., 2025c, preprint (arXiv:2506.14870)
Dalla Bontà E. et al., 2025, A&A, 696, A48
Dayal P. et al., 2025, A&A, 697, A211
Dayal P., 2024, A&A, 690, A182
Dayal P., Ferrara A., Dunlop J. S., Pacucci F., 2014, MNRAS, 445, 2545
Dayal P., Maiolino R., 2025, preprint (arXiv:2506.08116)
Dayal P., Rossi E. M., Shiralilou B., Piana O., Choudhury T. R., Volonteri M., 2019, MNRAS, 486, 2336
de Graaff A. et al., 2025, A&A, 701, A168
Dekel A. et al., 2025a, preprint (arXiv:2511.07578)
Dekel A., Stone N. C., Chowdhury D. D., Gilbaum S., Li Z., Mandelker N., van den Bosch F. C., 2025b, A&A, 695, A97
Dors O. L., Maiolino R., Cardaci M. V., Hägele G. F., Krabbe A. C., Pérez-Montero E., Armah M., 2020, MNRAS, 496, 3209
Escrivà A., Kühnel F., Tada Y., 2024, in Arca Sedda M., Bortolas E., Spera M., eds, Black Holes in the Era of Gravitational-Wave Astronomy. Elsevier, Amsterdam, p. 261
Euclid Collaboration, 2025, preprint (arXiv:2503.15323)
Furtak L. J. et al., 2023, ApJ, 952, 142
Furtak L. J. et al., 2024, Nature, 628, 57
Furtak L. J. et al., 2025, A&A, 698, A227
Geris S. et al., 2025, preprint (arXiv:2506.22147)
Greene J. E. et al., 2024, ApJ, 964, 39
Hainline K. N. et al., 2025, ApJ, 979, 138
Harikane Y. et al., 2023, ApJ, 959, 39
Hawking S., 1971, MNRAS, 152, 75
Henden N. A., Puchwein E., Shen S., Sijacki D., 2018, MNRAS, 479, 5385
Hopkins P. F., 2015, MNRAS, 450, 53
Hsiao T. Y.-Y. et al., 2025, preprint (arXiv:2505.03873)
Hviding R. E. et al., 2025, A&A, 702, A57
Inayoshi K., 2025, ApJ, 988, L22
Inayoshi K., Maiolino R., 2025, ApJ, 980, L27
Isobe Y. et al., 2025, MNRAS, 541, L71
Isobe Y., Ouchi M., Nakajima K., Harikane Y., Ono Y., Xu Y., Zhang Y., Umeda H., 2023, ApJ, 956, 139
Jeon J. et al., 2025a, preprint (arXiv:2508.14155)
Jeon J., Bromm V., Liu B., Finkelstein S. L., 2025b, ApJ, 979, 127
Ji X. et al., 2025a, MNRAS, 544, 3900
Ji X. et al., 2025b, preprint (arXiv:2507.23774)
Ji X. et al., 2025c, MNRAS, 541, 2134
Juarez Y., Maiolino R., Mujica R., Pedani M., Marinoni S., Nagao T., Marconi A., Oliva E., 2009, A&A, 494, L25
Juodžbalis I. et al., 2024a, MNRAS, 535, 853
Juodžbalis I. et al., 2024b, Nature, 636, 594
Juodžbalis I. et al., 2025a, preprint (arXiv:2504.03551)
Juodžbalis I. et al., 2025b, preprint (arXiv:2508.21748)
Katz N., Weinberg D. H., Hernquist L., 1996, ApJS, 105, 19
Kauffmann G. et al., 2003, MNRAS, 346, 1055
Kewley L. J., Heisler C. A., Dopita M. A., Lumsden S., 2001, ApJS, 132, 37
King A., 2025, MNRAS, 536, L1
Kobayashi C., Karakas A. I., Lugaro M., 2020, ApJ, 900, 179
Kocevski D. D. et al., 2023, ApJ, 954, L4
Kokorev V. et al., 2023, ApJ, 957, L7
Kokubo M., Harikane Y., 2024, ApJ, 995, id.24
Konstantopoulou C. et al., 2024, A&A, 681, A64
Koudmani S., Sijacki D., Smith M. C., 2022, MNRAS, 516, 2112
Lambrides E. et al., 2024, preprint (arXiv:2409.13047)
Laseter I. H. et al., 2024, A&A, 681, A70
Li J. et al., 2025, ApJ, 981, 19
Lin X. et al., 2025a, preprint (arXiv:2504.08039)
Lin X. et al., 2025b, preprint (arXiv:2507.10659)
Loiacono F. et al., 2025, A&A, 703, A36
Luridiana V., Morisset C., Shaw R. A., 2015, A&A, 573, A42
Ma Y. et al., 2025, ApJ, 981, 191
Madau P., Haardt F., 2024, ApJ, 976, L24
Maiolino R. et al., 2025, MNRAS, 538, 1921
Maiolino R. et al., 2024a, Nature, 627, 59
Maiolino R. et al., 2024b, A&A, 691, A145
Marconcini C. et al., 2023, A&A, 677, A58
Marconi A., Axon D. J., Maiolino R., Nagao T., Pastorini G., Pietrini P., Robinson A., Torricelli G., 2008, ApJ, 678, 693
Marconi A., Axon D. J., Maiolino R., Nagao T., Pietrini P., Risaliti G., Robinson A., Torricelli G., 2009, ApJ, 698, L103
Marshall M. A. et al., 2025, A&A, 702, A50
Matthee J. et al., 2024, ApJ, 963, 129
Mazzolari G. et al., 2025, A&A, 700, A12
Mazzolari G. et al., 2024a, preprint (arXiv:2412.04224)
Mazzolari G. et al., 2024b, A&A, 691, A345
Morishita T., Liu Z., Stiavelli M., Treu T., Bergamini P., Zhang Y., 2025, preprint (arXiv:2507.10521)
Mowla L. et al., 2024, Nature, 636, 332
Naidu R. P. et al., 2025, preprint (arXiv:2503.16596)
Nakajima K. et al., 2022, ApJS, 262, 3
Nakajima K. et al., 2025, preprint (arXiv:2506.11846)
Nakajima K., Maiolino R., 2022, MNRAS, 513, 5134
Nandal D., Buldgen G., Whalen D. J., Regan J., Woods T. E., Tan J. C., 2025, A&A, 701, A262
Natarajan P., Pacucci F., Ricarte A., Bogdán Á., Goulding A. D., Cappelluti N., 2024, ApJ, 960, L1
Netzer H., Shemmer O., Maiolino R., Oliva E., Croom S., Corbett E., di Fabrizio L., 2004, ApJ, 614, 558
Pacucci F., Ferrara A., Volonteri M., Dubus G., 2015, MNRAS, 454, 3771
Pacucci F., Narayan R., 2024, ApJ, 976, 96
Partmann C., Naab T., Lahén N., Rantala A., Hirschmann M., Hislop J. M., Petersson J., Johansson P. H., 2025, MNRAS, 537, 956
Piana O., Dayal P., Choudhury T. R., 2022, MNRAS, 510, 5661
Planck Collaboration VI, 2020, A&A, 641, A6
Prole L. R. et al., 2025, preprint (arXiv:2511.09640)
Qin W., Kumar S., Natarajan P., Weiner N., 2025, preprint (arXiv:2506.13858)
Rantala A., Lahén N., Naab T., Escobar G. J., Iorio G., 2025, MNRAS, 543, 2130
Rashed Y. E., Eckart A., Valencia-S. M., García-Marín M., Busch G., Zuther J., Horrobin M., Zhou H., 2015, MNRAS, 454, 2918
Reines A. E., Volonteri M., 2016, in American Astronomical Society Meeting Abstracts #227, p. 119.01
Rhea C. L. et al., 2025, AJ, 169, 203

Riotto A., Silk J., 2024, preprint (arXiv:2403.02907)
Rodríguez Del Pino B. et al., 2024, A&A, 684, A187
Rusakov V. et al., 2025, preprint (arXiv:2503.16595)
Sanati M. et al., 2025, MNRAS, 542, 1532
Sanders R. L. et al., 2025, preprint (arXiv:2508.10099)
Sanders R. L., Shapley A. E., Topping M. W., Reddy N. A., Brammer G. B., 2024, ApJ, 962, 24
Saslaw W. C., Valtonen M. J., Aarseth S. J., 1974, ApJ, 190, 253
Schneider R., Valiante R., Trinca A., Graziani L., Volonteri M., Maiolino R., 2023, MNRAS, 526, 3250
Scholte D. et al., 2025, MNRAS, 540, 1800
Scholtz J. et al., 2025, A&A, 697, A175
Sijacki D., Vogelsberger M., Genel S., Springel V., Torrey P., Snyder G. F., Nelson D., Hernquist L., 2015, MNRAS, 452, 575
Springel V., Hernquist L., 2003, MNRAS, 339, 289
Stone M. A., Lyu J., Rieke G. H., Alberts S., Hainline K. N., 2024, ApJ, 964, 90
Strom A. L., Steidel C. C., Rudie G. C., Trainor R. F., Pettini M., Reddy N. A., 2017, ApJ, 836, 164
Tan J. C., Singh J., Cammelli V., Sanati M., Petkova M., Nandal D., Monaco P., 2024, preprint (arXiv:2412.01828)
Taylor A. J. et al., 2025a, ApJ, 986, 165
Taylor A. J. et al., 2025b, ApJ, 989, L7
Topping M. W. et al., 2025, ApJ, 980, 225
Trac H., Cen R., Mansfield P., 2015, ApJ, 813, 54
Trefoloni B. et al., 2025, A&A, 700, A203
Trinca A. et al., 2024a, preprint (arXiv:2412.14248)
Trinca A., Schneider R., Maiolino R., Valiante R., Graziani L., Volonteri M., 2023, MNRAS, 519, 4753
Trinca A., Schneider R., Valiante R., Graziani L., Ferrotti A., Omukai K., Chon S., 2024b, MNRAS, 529, 3563
Trinca A., Schneider R., Valiante R., Graziani L., Zappacosta L., Shankar F., 2022, MNRAS, 511, 616
Tripodi R. et al., 2024, Nature Communications, 16, id.9830
Übler H. et al., 2023, A&A, 677, A145
Übler H. et al., 2024, MNRAS, 531, 355
Valiante R., Schneider R., Volonteri M., Omukai K., 2016, MNRAS, 457, 3356
Vanzella E. et al., 2023, A&A, 678, A173
Vanzella E. et al., 2025, preprint (arXiv:2509.07073)
Vogelsberger M. et al., 2014, MNRAS, 444, 1518
Vogelsberger M., Genel S., Sijacki D., Torrey P., Springel V., Hernquist L., 2013, MNRAS, 436, 3031
Volonteri M., Haardt F., Madau P., 2003, ApJ, 582, 559
Wang B. et al., 2025, ApJ, 984, 121
Wang S. et al., 2022, ApJ, 925, 121
Wiersma R. P., Schaye J., Smith B. D., 2009a, MNRAS, 393, 99
Wiersma R. P., Schaye J., Theuns T., Dalla Vecchia C., Tornatore L., 2009b, MNRAS, 399, 574
Willott C. J. et al., 2025, ApJ, 988, 26
Yue M., Eilers A.-C., Ananna T. T., Panagiotou C., Kara E., Miyaji T., 2024, ApJ, 974, L26
Zhang B., Feng W.-X., An H., 2025, preprint (arXiv:2507.07171)
Zhang S., Bromm V., Liu B., 2024, ApJ, 975, 139
Zhang S., Liu B., Bromm V., Jeon J., Boylan-Kolchin M., Kühnel F., 2025, ApJ, 987, 185
Zhang Z., Jiang L., Liu W., Ho L. C., 2025, ApJ, 985, 119
Ziparo F., Gallerani S., Ferrara A., 2025, J. Cosmol. Astropart. Phys., 2025, 040
Ziparo F., Gallerani S., Ferrara A., Vito F., 2022, MNRAS, 517, 1086

APPENDIX A: RULING OUT THE HIGH-METALLICITY SOLUTION

As discussed in the main text, for a given [O III]/Hβ ratio the metallicity calibration has two solutions, as illustrated in Fig. 4. Therefore, in principle, the [O III]/Hβ value observed in QSO1 could also correspond to extremely high metallicity, more than three times solar. Such an extremely high metallicity would be totally implausible for such a low-mass system at such high redshift (e.g. M. Curti et al. 2024). Additionally, the high-metallicity solution can be ruled out based on the upper limits on the low-ionization lines. Indeed, as illustrated in Fig. A1 (top), [O II]3727 is not detected. The ratio [O III]/[O II] has a monotonic dependence on metallicity, which has also been calibrated for high-z galaxies (R. L. Sanders et al. 2024; E. Cataldi et al. 2025), as shown in Fig. A2 (top). The lower limit on the [O III]/[O II] ratio in QSO1 implies a metallicity $< 0.4\ Z_\odot$, hence completely ruling out the supersolar solution of [O III]/Hβ. The [S II]6716,6731 doublet is also undetected (Fig. A1), and the upper limit on [S II]/Hα is also informative. Indeed, M. Curti et al. (2020) showed that the ratio $O3S2 = \frac{[O\,\mathrm{III}]/\mathrm{H}\beta}{[S\,\mathrm{II}]/H\alpha}$ is monotonically decreasing with metallicity. Unfortunately, this diagnostic has not been calibrated at high-z. However, using the local relation, shown in Fig. A2 (bottom,) and the 3σ lower limits obtained for QSO1 reported in Table 1, we obtain an upper limit on the metallicity of $< 0.7\ Z_\odot$, once again excluding the highly supersolar metallicity solution of [O III]/Hβ.

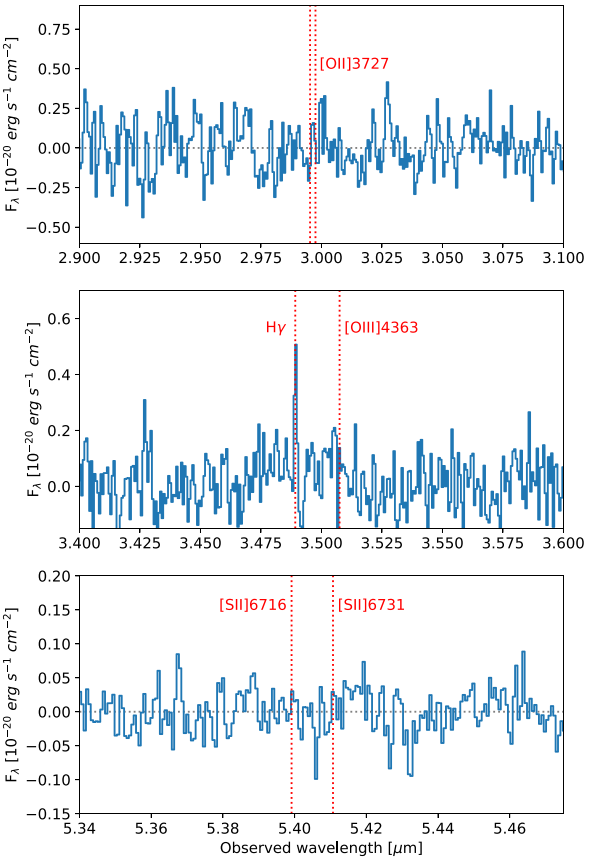

Figure A1. Portion of spectra extracted from the central aperture illustrating the non-detections of [O II]3727, [O III]4363, and [S II]6716,6731.

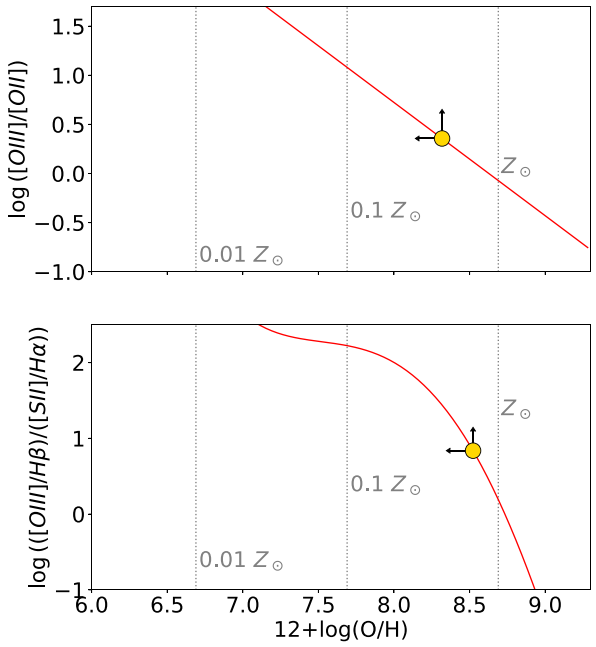

Figure A2. Constraints on the metallicity from the non-detection of low-ionization lines. Top: log([O III]5007/[O II]3727) lines flux ratio versus metallicity according to the calibration obtained by R. L. Sanders et al. (2024) at high-z (red line). Bottom: log(([O III]5007/Hβ)/([S II]6716,6731/Hα)) as a function of metallicity according to the local relation identified by M. Curti et al. (2020). In both panels, the symbols indicate the 3σ limits obtained for QSO1, both of which exclude the highly supersolar metallicity solution of the [O III]/Hβ value.

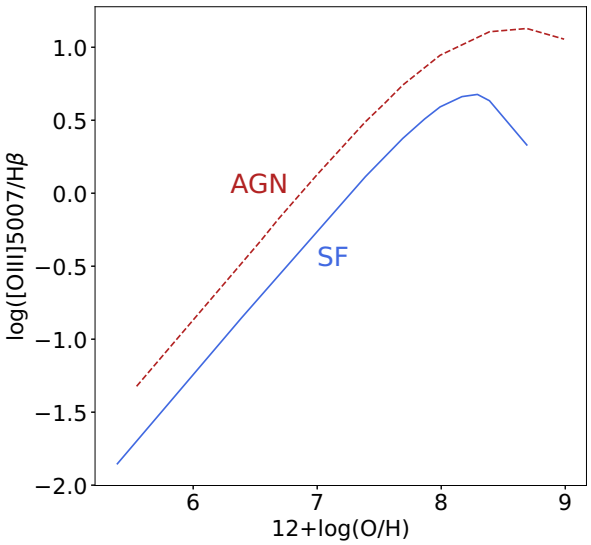

Figure B1. [O III]5007/Hβ flux ratio as a function of metallicity for AGN (red dashed) and star formation (blue solid) models, as discussed in the text. In the low-metallicity (subsolar) branch, a given [O III]/Hβ ratio resulting AGN photoionization would result into a metallicity even lower than inferred for the star formation case.

APPENDIX B: THE CASE OF AGN EXCITATION OF THE NARROW LINES

In the main text we have assumed, following F. D'Eugenio et al. (2025b), that the narrow emission lines are excited by star formation. F. D'Eugenio et al. (2025b) motivated this by the extremely narrow width of the lines. Here, we discuss the scenario in which the narrow lines are excited by the AGN, i.e. are part of an NLR, although in this case one would expect broader lines because of feedback from AGN radiation pressure.

The calibration obtained by E. Cataldi et al. (2025) for high-z star-forming galaxies is not expected to change significantly in the case of AGN. Indeed, high-z galaxies are characterized by very high-ionization parameters, similar to the AGN, and tend to have harder ionizing spectrum than local galaxies, akin AGN, because of their reduced iron content (A. L. Strom et al. 2017; A. J. Cameron et al. 2024). At the same time, high-z AGNs are characterized by softer ionizing spectra than local AGN, akin star-forming galaxies, as indicated by the weakness of high-ionization lines (E. Lambrides et al. 2024). Therefore, the physical conditions and ionization of high-z star-forming galaxies and the NLR of high-z AGN are expected to be similar. Indeed, it is known that in many traditional narrow-line diagnostic diagrams, high-z AGN and high-z SF galaxies largely overlap (H. Übler et al. 2023; R. Maiolino et al. 2024b; I. Juodžbalis et al. 2025a); this makes the identification of narrow-line (type 2) AGN extremely difficult at high-z (G. Mazzolari et al. 2024a; J. Scholtz et al. 2025) and indeed the high-z sample used by E. Cataldi et al. (2025, and compilation in there) for the calibrations, may include a few high-z AGN according to some diagnostics. Therefore, the low metallicity inferred from the E. Cataldi et al. (2025) calibration may likely hold also in the case of AGN photoionization of the narrow lines.

In any case, the harder ionization spectrum from an AGN would make the [O III]/Hβ ratio even higher at a given metallicity, relative to star-forming galaxies. We illustrate this in Fig. B1, where we show the example of the expected [O III]/Hβ ratio in the case of an AGN ionizing spectrum (red dashed) and a star formation ionizing spectrum (blue solid), for a given ionization parameter $\log U = -2$. We use the models presented in K. Nakajima & R. Maiolino (2022), where for the AGN we take the case of an ionizing spectrum modelled with a blackbody with temperature 2×10^5 K and power law $\alpha = -2$, while the BPASS models with age 1Myr age used for star-forming galaxies. Clearly, in the low-metallicity branch, in case of AGN photoionization a given [O III]/Hβ ratio would give an even lower metallicity than inferred by assuming photoionization by star formation.

APPENDIX C: RULING OUT HIGH-DENSITY SCENARIO FOR THE WEAKNESS OF [O III]

The lack of a broad component of [O III]5007 is expected, as the gas density in the BLR ($n \sim 10^9 - 10^{12}$ cm^{-3}) is much higher than the critical density of this transition ($n_c = 7 \times 10^5$ cm^{-3}), hence this line is collisionally de-excited in the BLR, relative to Hβ. The weakness of [O III]5007 relative to the *narrow* component of Hβ is instead much more difficult to explain, and actually unphysical, in a high-density scenario, as discussed in the following.

Although the densities of the ionized ISM are found, on average, to increase in high-z galaxies, they are still found to be below $< 10^5$ cm^{-3} (Y. Isobe et al. 2023; M. W. Topping et al. 2025, one case found to have $n > 10^6$ cm^{-3} has actually been ascribed to the BLR of an AGN, with $n \sim 10^{10}$ cm^{-3}; R. Maiolino et al. 2024a). In any case, we can directly provide constraints on the density of the gas in the ionized gas of QSO1 that produces the narrow lines. We focus on the spectrum extracted from the central aperture ($R < 150$ pc); the arguments would be even stronger for the larger aperture. We assume

a radial density distribution following a power law

$$n(r) = n_0 \left(\frac{r}{r_0}\right)^{-\alpha}$$

where n_0 is the density at a reference radius r_0. We take $r_0 = 100$ pc, i.e. well within the aperture. We also assume that the clouds with such a density profile have a filling factor f defined as

$$f = \frac{V_{clouds}}{V_{tot}} = \frac{N_{clouds} R_c^3}{R_{max}^3}$$

where $V_{\rm tot}$ is the volume enclosed in the aperture, assumed spherical with radius $R_{\rm max}$, $V_{\rm clouds}$ is the volume occupied by the ionized clouds, and $N_{\rm clouds}$ is the number of clouds and R_c is their radius. The mass of gas contained within the aperture is given (assuming a medium made only of hydrogen for simplicity)

$$M_g = \int_{R_{min}}^{R_{max}} n(r) m_p f 4\pi r^2 dr$$

where m_p is the proton mass. For $R_{\rm min}$ we take 5 pc, as smaller radii would make the line broader because they would be completely within the sphere of influence of the BH; we however note that selecting even smaller inner radii would make the arguments even stronger. The blue solid lines in Fig. C1 show the implied gas mass as a function of density for different values of the filling factor f. We also indicate with labels, for each filling factor, the implied maximum size of the clouds obtained by assuming the extreme case that all gas is contained in a single cloud ($N_{\rm clouds} = 1$), while in reality the clouds would be much smaller. We then derive the mass of ionized gas inferred from the luminosity of Hβ_N

$$\frac{M_{ion}}{M_\odot} = 10^9 \frac{L(H\beta_N)}{10^{43} ergs^{-1}} \frac{100 cm^{-3}}{n_0} \frac{3-2\alpha}{3-\alpha} r_0^{-3\alpha} \frac{R_{max}^{3-\alpha} - R_{min}^{3-\alpha}}{R_{max}^{3-2\alpha} - R_{min}^{3-2\alpha}}$$

We have assumed a temperature $T = 10\,000$ K, the results would be even tighter if assuming a higher temperature. The resulting constraint on the mass of ionized gas is shown with a red solid line in Fig. C1, in the case of $\alpha = 2$. We also show the extreme (unlikely) case of $\alpha = 0$ (i.e. uniform distribution) with a red dashed line. In order for the gas to have a density higher than 10^6 cm^{-3} (vertical black dotted line), at which [O III]5007 starts to be collisionally suppressed by a factor of 1.5 (which would still not affect significantly our results) the ionized clouds should have an extremely small filling factor ($f < 10^{-8} - 10^{-10}$) and should have sizes even smaller than stars. We have used CLOUDY models to infer that, in order to suppress [O III]5007 by a factor of 10, which would be needed to entirely ascribe to collisional de-excitation the lower [O III]/Hβ ratio relative to the other AGN and galaxies at $z \sim 7$, the ISM would need to reach densities higher than 10^7 cm^{-3}. As illustrated in Fig. C1 (dot–dashed vertical black line), this would require even more extreme filling factors and clouds as small as planets.

Finally, we note that the non detection of [O III]4363 (as illustrated in Fig. A1), which has a critical density much higher than [O III]5007, also rules out very high densities. Indeed, Fig. C2 illustrates the variation of [O III]4363/[O III]5007 as a function of temperature and density, estimated with the PYNEB software (V. Luridiana, C. Morisset & R. A. Shaw 2015). For reasonable temperatures typical of the photoionized gas emitting Hβ ($T > 10^4$ K), the inferred upper limit in the central region ([O III]4363/[O III]5007<0.33, Table 1) gives an upper limit on the density of $n < 10^7$ cm^{-3}.

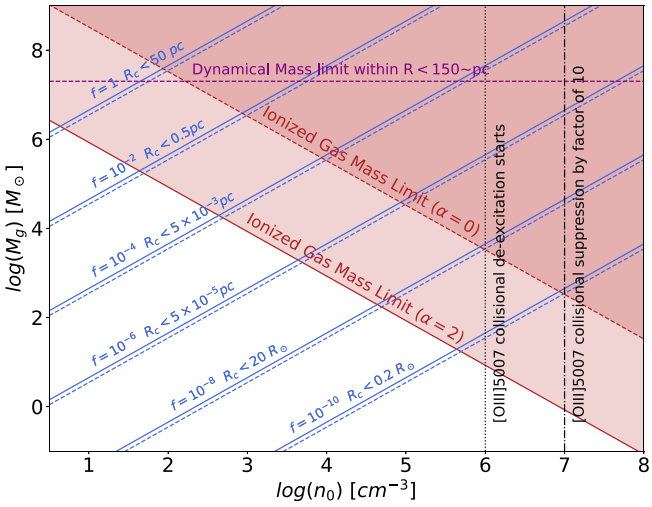

Figure C1. Constraints on the gas density for the gas emitting the narrow emission lines. The blue lines indicate the gas mass enclosed within the central aperture for as a function of gas density n_0 at $R = 100$ pc, for a power-law radial distribution $n \propto r^{-\alpha}$ with index $\alpha = 2$ (solid) and $\alpha = 0$ (dashed), for different filling factors (and implied upper limits on the clouds size) as labelled. The red lines indicate the mass of ionized gas constrained by the Hβ_N luminosity for the two power indices. The vertical dotted line indicates the density where collisional de-excitation of [O III]5007 starts to affect its flux by ~ 50 per cent, the dot–dashed line is the density required to suppress the flux by a factor of 10. Explaining the weakness of [O III]5007 via collisional de-excitation would require extremely low filling factors and clouds smaller than stars. The horizontal purple line indicates the upper limit given by the dynamical mass inferred by I. Juodžbalis et al. (2025b).

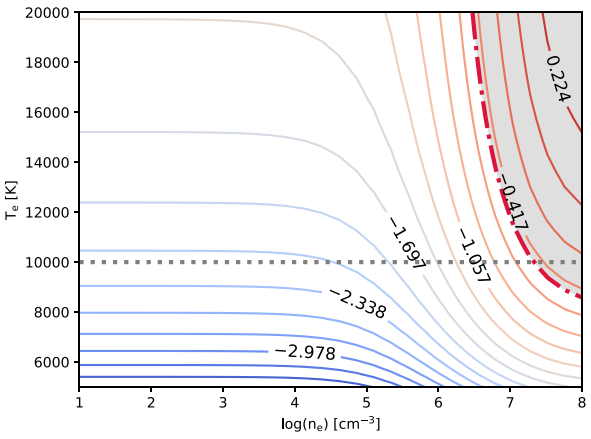

Figure C2. [O III]4363/[O III]5007 flux ratio as a function of temperature and density. The observed upper limit [O III]4363/[O III]5007<0.33 is marked with a thick dot–dashed line and indicate densities $< 10^7$ cm^{-3} for reasonable temperatures $T > 10^4$ K.

APPENDIX D: RULING OUT PECULIAR IONIZATION SCENARIOS FOR THE [O III] WEAKNESS

In principle, another scenario to explain the weakness of [O III] relative to Hβ, without invoking low metallicity and in the low-density regime, is that the gas ionization state is so low that O^{+2} is not produced. This would happen if the ionization parameter $U = Q_i/(4\pi r^2 nc)$ (where Q_i is the rate of ionizing photons) is very

low, much lower than typically observed in other galaxies. This would be in contrast with the finding that high-z galaxies are characterized by higher ionization parameters than lower redshift galaxies (A. J. Cameron et al. 2024).

Additionally, a low-ionization parameter would result in a relatively strong [O II]3727 emission, which is not detected (Appendix A). We have quantified the latter argument more in detail by using CLOUDY photoionization modelling. We have inferred that (assuming an AGN Spectral Energy Distribution, SED), in the low-density regime for the ISM ($n < 10^4$ cm^{-3}, which gives reasonable filling factors and cloud sizes, Fig. C1), the lower limit on $F([\mathrm{O\,III}]5007)/F([\mathrm{O\,II}]3727) > 3$ (by also conservatively taking into accounting an extinction of $A_V = 0.66$) requires an ionization parameter $\log\ U > -2.78$. With such a constraint on the ionization parameter it is not possible to reproduce the observed low [O III]/Hβ ratio with the typical metallicity observed in other high-z galaxies of $Z \sim 0.1\ Z_\odot$. Reproducing the observed [O III]/Hβ ratio, while maintaining $\log\ U > -2.78$, requires lowering the metallicity, with an upper limit of $\log(Z/Z_\odot) < -1.7$, i.e. close to the value inferred from the calibrations.

It is also possible to exclude a low-ionization parameter solution based on simple geometrical arguments and based on the gas distribution. The source of UV radiation powering the narrow line (be it AGN or star formation) is unresolved, and confined within $r < 30$ pc (L. J. Furtak et al. 2024). For simplicity, and conservatively, we assume it to be point-like. From the Hα luminosity (corrected for extinction) we infer a production of ionizing photons $Q_i = 1.4 \times 10^{54}$ s^{-1}. The surface brightness profile within the central aperture is not resolved. However, assuming, as in the previous appendix, a typical power-law density profile with power index of -2, the luminosity weighted radius within the aperture is 77 pc. Conservatively assuming an upper limit on the density of $n < 10^4$ cm^{-3} we obtain a lower limit on the ionization parameter of $\log\ U > -2.2$. With such a high value of the ionization parameter, suppressing [O III] to the observed value of [O III]/Hβ would require a metallicity $Z < 10^{-1.9}\ Z\odot$.

A similar scenario for explaining the low [O III]/Hβ could be that, without invoking low metallicity, the ionizing spectrum is deficient in photons energetic enough to ionize O^+. However, this scenario would not explain the absence of [O II], as oxygen has about the same ionization potential as hydrogen. Similarly, [N II] and [S II] should be quite strong (C. L. Rhea et al. 2025).

The opposite scenario would be that the ionization of the gas is so high that oxygen is mostly in O^{+3}. However, it has never been seen, not even in the most extreme AGN, that the ionization of the gas is so high to suppress [O III] emission (O. L. Dors et al. 2020). In any case, such a high level of ionization would result in other high-ionization lines, such as C IV and He II, to be very strong. In particular, using CLOUDY modelling, we infer that in order to make [O III]/Hβ as faint as observed, while keeping the metallicity $\log(Z/Z_\odot) > -1.5$ and assuming an AGN ionizing spectrum, it would require an extremely high-ionization parameter, higher than about unity. In such conditions, He IIλ4686 should be about as strong as [O III], or even stronger, while He II is undetected.

APPENDIX E: BPT DIAGNOSTIC DIAGRAMS

In principle having information on the [O III]/Hβ we could locate QSO1 on the classical excitation diagnostic diagrams, such as the J. A. Baldwin, M. M. Phillips & R. Terlevich (1981). These diagrams have turned out to be much less discriminatory of the galaxy properties at high redshift, and in particular the distinction between AGN and star-forming galaxies. Indeed, at $z > 4$ AGN have found to mostly overlap with star-forming galaxies, an effect which has mostly been ascribed to the lower metallicity of the NLR (e.g. H. Übler et al. 2023; R. Maiolino et al. 2024b; I. Juodžbalis et al. 2025a), an issue that has prompted the development of alternative diagnostics based on fainter optical lines or UV lines (e.g. G. Mazzolari et al. 2024b; J. Scholtz et al. 2025). In the case of QSO1, the BPT diagarms are even more problematic as the low-ionization lines that are required to locate the source are not detected, and the upper limit are not very informative, as discussed in the following.

The left panel of Fig. E1 shows the so-called [N II]–BPT diagram, i.e. [O III]5007/Hβ_N versus [N II]6584/Hα_N, where contours show the distribution of local galaxies and the solid black line indicates the limit for maximal starburst identified by L. J. Kewley et al. (2001),

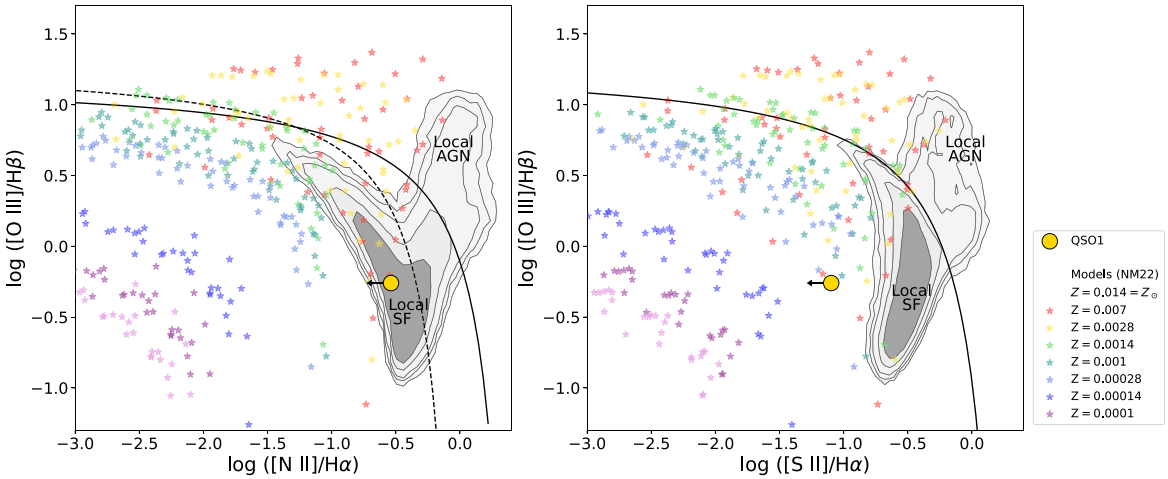

Figure E1. BPT emission-line ratio diagnostic diagrams (J. A. Baldwin et al. 1981). Left: log([O III]5007/Hβ) versus log([N II]6584/Hα). Right: log([O III]5007/Hβ) versus log([S II]6716,6731/Hα). In both diagrams, contours show the distribution of local galaxies. The solid black line indicates the limit for maximal starburst identified by L. J. Kewley et al. (2001), while the black dashed line is the local demarcation between star-forming galaxies and AGN identified by G. Kauffmann et al. (2003). Small starred symbols are AGN photoionization models from K. Nakajima & R. Maiolino (2022) spanning different densities and ionization parameters, and colour-coded by metallicity. The circle is the observation of QSO1 (central region), for which only relatively loose upper limits are available on [N II]/Hα and [S II]/Hα, although the latter already excludes most high-metallicity models.

while the black dashed line is the local demarcation between star-forming galaxies and AGN identified by G. Kauffmann et al. (2003). F. D'Eugenio et al. (2025b) provide an upper limit of 0.29 on the ratio [N II]/Hα in QSO1 (Table 1). This upper limit, together with our the [O III]/Hβ ratio inferred in our work, is shown with a golden circle. The starred small symbols are from the AGN photoionization models presented in K. Nakajima & R. Maiolino (2022), which span a wide range of ionization parameters, ionizing spectrum shapes, and colour coded by metallicity as indicated in the legend. Clearly, the current upper limit on [N II]/Hα is not very constraining, except for indicating that QSO1 is not located in the local AGN locus, as is the case for many other AGN at high-z.

The right panel of Fig. E1 shows the so-called [S II]–BPT diagram, where [N II] is replaced by the flux of the [S II]6717,6731 doublet. In this case, we report the [S II]/Hα inferred in our work (Table 1 and Appendix D). In this case, the location of QSO1 is somewhat more constraining. It indicates that the location of QSO1 is not only inconsistent with local AGN, but also inconsistent with the locus of local star-forming galaxies. Additionally, when compared with photoionization models by K. Nakajima & R. Maiolino (2022), it indicates that it is mostly inconsistent with metallicities higher than $\sim 2.8 \times 10^{-3}$, i.e. $Z < 2 \times 10^{-2}$, although the upper limit could be marginally consistent with some rare cases of high-metallicity models.

APPENDIX F: VARIABILITY

Because of the different traveltimes, the three lensed images of QSO1 are observed at different epochs. Specifically, image C is followed by image A 18–19 yr later (i.e. 2.2–2.4 yr later in the rest frame), and this is then followed by image B another 2.2–3 yr later (i.e. 3.2–4.5 months later in the rest frame). Therefore, the three images offer, in principle, the possibility of investigating the AGN variability on different time-scales. However, simply comparing the fluxes of the three images (corrected for magnification) does not provide a robust method to explore variability, due the uncertainties in the lens magnification of each of the three images. Yet, variability between the three images can be explored in terms of Equivalent Width (EW) of the emission lines, as this quantity is independent of the magnification factor. Indeed, both X. Ji et al. (2025a) and L. J. Furtak et al. (2025) have reported that the EW of Hβ and Hα in image C of QSO1 is significantly larger than in images A and B. X. Ji et al. (2025a) interpret this variation in terms of a decrease of the accretion disc continuum to which the BLR has not yet reacted, because of time delay; this interpretation is also supported by the lower continuum observed in the spectroscopic observation relative to photometric data of the same image obtained one year earlier.

Having evidence that QSO1 is variable, one may wonder whether variability may play a role in the observed narrow-line ratios. We have seen that the narrow lines are emitted on scales of a few 100 pc, hence even if they are ionized by the AGN (and not by star formation), they are not sensitive to AGN continuum variability on time-scales shorter than a few 100 yr. However, it is possible that the currently observed narrow lines were excited by the AGN at an epoch when it was experiencing different rates of accretion, hence producing higher or lower ionizing radiation. While this can certainly modulate the absolute intensity of the lines, is not obvious that this could affect the line ratios; in particular, both Hβ_N and [O III] would brighten or become fainter together, proportionally. One possibility is that the dimming of the ionizing radiation may have been so extreme that could have resulted in an extremely low-ionization parameter, which may have produced a very low [O III]/Hβ; however, the low-ionization parameter scenario is ruled out in Appendix D on various grounds.

Another possibility is that the different narrow lines may react on different time-scales to the long-term variations of the continuum ionizing emission, possibly because of large-scale stratification of the emitting regions. This has been observed in some nearby AGN (Y. E. Rashed et al. 2015). However, even in the most extreme cases, the differential temporal variation of the [O III] and Hβ lines is only 10–15 per cent, which would certainly not account for the very low [O III]/Hβ observed in QSO1, a factor of a few/several lower than other (chemically evolved) AGN at lower redshifts.

APPENDIX G: SEMI-ANALYTICAL MODELS AND HYDRODYNAMICAL SIMULATIONS

In this section, we provide additional information on the SAMs and hydrodynamical simulations that have been used in Fig. 5.

G1 DELPHI

DELPHI is an SAM that uses a binary merger tree approach to jointly track the build-up of dark matter haloes, their baryonic components (gas, stellar, dust, and metal masses) and BHs at $z >= 4.5$ (P. Dayal et al. 2014, 2019, 2025; O. Piana, P. Dayal & T. R. Choudhury 2022) using the Planck 2020 cosmological model (Planck Collaboration VI 2020). We follow the assembly of dark matter haloes between $\log_{10}(M_{\rm h}/{\rm M}_\odot) = 8 - 14$ from $z \sim 40$ down to $z = 4.5$ with a mass resolution of $10^8\,{\rm M}_\odot$. Crucially, this model has been calibrated against the latest data sets for both star-forming galaxies and BHs assimilated by the *JWST* and the Atacama Large Millimetre Array (ALMA), and run exploring: (i) different seeding prescriptions including *light* ($100\,{\rm M}_\odot$) and *heavy* seeds ($10^{3-5}\,{\rm M}_\odot$); (ii) different spins exploring cases with spin values of $s = 0, +1, -1$; and (iii) allowing BH growth in both EL and SE accretion scenarios. In this model, the growth of BHs is regulated both by the host halo mass and the gas mass left after star formation and the associated Type II supernova (SNII) feedback. Our model includes a 'critical' halo mass for efficient BH accretion with a value that evolves with redshift as $M_{\rm bh}^{\rm crit}(z) = 10^{11.25}[\Omega_m(1+z)^3 + \Omega_\Lambda]^{-0.125}$ on which we include a scatter of 0.5 dex, motivated by the results of cosmological simulations (R. G. Bower et al. 2017). In order to explain the number density of *JWST*-detected AGN, at any time-step BHs are allowed to accrete a gas mass of $M_{\rm bh}^{\rm crit}(z) = \min[\epsilon_r f_{\rm bh}^{\rm ac} M_{\rm g}^{\rm sf}, f_{\rm Edd}\, m_{\rm Edd}]$ where $M_{\rm g}^{\rm sf}$ is the gas mass left after star formation and its associated SNII feedback, $f_{\rm Edd}$ is the Eddington fraction, and $m_{\rm Edd}$ is the Eddington accretion rate. Allowing very weak AGN feedback (0.01 per cent of BHs feedback coupling to the gas) we require values of $f_{\rm bh}^{\rm ac} = 0.1$ (5×10^{-4}) and $f_{\rm Edd} = 1.0$ (10^{-4}) for haloes above (below) the critical mass (we allow 0.5 dex of scatter on all of these quantities); i.e. BHs in high-mass (low-mass) haloes can accrete the minimum between 10 per cent (0.05 per cent) of the available gas mass and 100 per cent (0.01 per cent) of the Eddington fraction. Assuming instantaneous recycling and perfect mixing of gas, dust, and metals, we model the interlinked dust and metal contents of early systems including all of the relevant processes: for dust we account for production in SNII, destruction in SNII shocks, astration into star formation, ejection in outflows and grain growth in the cold ISM. The time evolution of metal enrichment is calculated as

$$\frac{{\rm d}M_{\rm Z}}{{\rm d}t} = \dot{M}_{\rm Z}^{\rm pro} - \dot{M}_{\rm Z}^{\rm ast} + \dot{M}_{d}^{\rm des} - \dot{M}_{\rm Z}^{\rm eje} - \dot{M}_{d}^{\rm gro}. \quad \text{(G1)}$$

where the terms on the right-hand side account for the rate of metal production ($\dot{M}_Z^{\rm pro}$) including the latest state-of-the-art yields from Type Ia SN (SNIa), SNII, and asymptotic giant branch (AGB) stars from C. Kobayashi, A. I. Karakas & M. Lugaro (2020), the rate of metals astrated into star formation ($\dot{M}_Z^{\rm ast}$), the rate of dust mass destruction in SNIII shocks that adds to the metal content ($\dot{M}_d^{\rm des}$), the rate of metals lost in outflows ($\dot{M}_Z^{\rm eje}$) and the rate of metals lost to dust grain growth in the cold ISM ($\dot{M}_d^{\rm gro}$). This model has already been used to study the contribution of BHs to the reionization process (P. Dayal et al. 2025) and been pushed to its extreme limits to explain the enormous BH-to-stellar mass ratios being observed with the *JWST* (L. J. Furtak et al. 2024).

G2 CAT

The CAT (A. Trinca et al. 2022, 2023) is a versatile SAM designed to trace and reproduce the early galaxy evolution during the first Gyr of cosmic history. Its primary goal is to explore how different formation and accretion scenarios for the first BH seeds contribute to the build-up of the massive BH population, as well as their co-evolution with host galaxies over cosmic time. CAT runs on a suite of semi-analytical dark matter merger trees, offering a large statistical sampling of the galaxy population from $z \approx 25$ down to $z = 4$. It resolves the formation of the first cosmic structures, with a minimum halo mass resolution of $\sim 10^6\,{\rm M}_\odot$, following the hierarchical assembly of dark matter haloes up to $\log(M_h/{\rm M}_\odot) = 14$. In each halo, CAT characterizes the formation of both PopIII and PopII stars, depending on the galaxy metallicity (A. Trinca et al. 2024b). The code then self-consistently tracks the enrichment of the ISM with dust and metals from both SNe and AGB stars, relying on mass- and metallicity-dependent stellar yields. The model include a two-phase ISM, where dust grains can be destroyed by SN shocks in the diffuse hot medium or grow in mass by accreting gas-phase metals in warm, dense gas. Mechanical feedback from SN explosions and AGN accretion is also included, potentially driving energy-driven galaxy-scale winds (R. Valiante et al. 2016). The enrichment of IGM is evolved across different merger trees, consistently with the predicted galaxy outflows. It is worth noting though that, due to the lack of spatial information on the DM halo distribution (which is an intrinsic limitation of our semi-analytical merger trees) the IGM metallicity is modelled as an average quantity. This value evolves with redshift and depends on the simulated overdensity. In reality, the patchy IGM enrichment might translate in lower metallicity levels than those predicted by the model for systems evolving in relative isolation.

The BH formation is implemented following two different seeding channels: *light seeds* ($M_{\rm seed} \sim 100\,{\rm M}_\odot$) form as remnants of PopIII stars, (formed in galaxies with metallicity below a critical threshold of $Z_{\rm crit} = 10^{-3.8}\,Z_\odot$). When the stellar population evolves, the most massive BH remnant formed is retained as the galaxy nuclear BH. *Heavy seeds* ($M_{\rm seed} = 10^5\,{\rm M}_\odot$) are assumed to form instead through the so-called direct collapse scenario (V. Bromm & A. Loeb 2003; M. C. Begelman, M. Volonteri & M. J. Rees 2006), under specific conditions for the host galaxy. The host halo must be metal-poor ($Z < Z_{\rm crit}$), support atomic hydrogen cooling ($T_{\rm vir} > 10^4$ K), and be exposed to a sufficiently strong Lyman–Werner (LW) radiation to suppress molecular hydrogen formation and prevent gas fragmentation, enabling the monolithic collapse of the gas. This last condition corresponds to a critical LW flux threshold of $J_{\rm LW} = 300\,J_{21}$, where $J_{21} = 10^{-21}\,{\rm erg\,s^{-1}\,cm^{-2}\,sr^{-1}\,Hz^{-1}}$.

The catalogues presented in this work consider two distinct accretion scenarios driving the subsequent BH growth (A. Trinca et al. 2022). In the EL model, nuclear BHs grow at the H. Bondi (1952) rate, with accretion capped at the EL. Due to the strong dependence of the Bondi rate on BH mass, light seeds are unable to grow significantly in this scenario. As a result, the massive BH population at high redshift originates exclusively from heavy seed progenitors. In the SE model, on top of the Bondi accretion, we allow for short episodes of enhanced accretion during major galaxy mergers (with typical durations of $\Delta t \sim 1\,{\rm Myr}$; A. Trinca et al. 2024a). These bursts are assumed to be driven by strong gas inflows into the nuclear region, triggered by angular momentum loss during mergers. During these phases, the BH accretion rate is modelled as $\dot{M}_{\rm BH} = \epsilon_{\rm BH} M_{\rm gas}/\tau_{\rm bulge}$, i.e. proportional to the galaxy gas content and independent of BH mass. These episodes of enhanced accretion are often characterized by SE rates, particularly for low-mass BHs, enabling light seeds to grow efficiently already at early times. Therefore, in this scenario, both light and heavy seeds contribute to the build-up of the massive BH population, with rapidly growing light seeds representing a competitive channel to the direct collapse scenario.

G3 AESOPICA

AESOPICA is a new suite of large-volume cosmological simulations (Koudmani et al., in preparation) built upon the FABLE galaxy formation model (N. A. Henden et al. 2018). The FABLE subgrid models are largely based on the ILLUSTRIS galaxy formation model (M. Vogelsberger et al. 2014). Whilst the models for star formation (V. Springel & L. Hernquist 2003), radiative cooling (N. Katz, D. H. Weinberg & L. Hernquist 1996; R. P. Wiersma, J. Schaye & B. D. Smith 2009a), and chemical enrichment (R. P. Wiersma et al. 2009b) are unchanged from ILLUSTRIS, the stellar feedback (M. Vogelsberger et al. 2013), and AGN feedback (D. Sijacki et al. 2015) models have been updated to include thermal stellar feedback and an AGN duty cycle. AESOPICA introduces additional targeted updates for modelling the growth of infant BHs in the early Universe, exploring three key modifications to fiducial galaxy formation models: enabling efficient accretion in the low-mass regime (S. Koudmani et al. 2022), incorporating SE accretion, and examining a broad range of seed masses (10^2 to $10^5\,{\rm M}_\odot$) following seed evolution from early cosmic epochs ($z \sim 20$). This is achieved by lowering the halo mass threshold for seeding BHs to the smallest resolvable halo size to $3 \times 10^9\,{\rm M}_\odot$. We note that this represents a likely optimistic seeding scenario, so our BH occupation for resolved haloes should be seen as an upper limit.

G4 PHANES: an analytic formalism for primordial black holes

We use the results obtained within the context of the PHANES analytic formalism. This is described in detail in P. Dayal & R. Maiolino (2025). This work follows the time evolution of galaxies seeded by PBHs. It purely focuses on the 'seed effect' where the Coulomb effect of a single BH can generate an initial density fluctuation that grows through gravitational instability (B. Carr & J. Silk 2018; A. Escrivà et al. 2024). BHs start accreting dark matter linearly starting at the redshift of matter-radiation equality ($z \sim 3400$) such that by $z \sim 34$, the dark matter halo starts dominating the potential. At this point, the halo is allowed to grow non-linearly using the accretion rate from state-of-the-art *N*-body simulations (H. Trac, R. Cen & P. Mansfield 2015). A halo is allowed to accrete gas – at a rate driven by the cosmological baryon-to-dark matter ratio – once its mass is

sufficient to host a baryonic overdensity of about 200. This gas can be accreted onto the BH to allow its growth, and form stars. The PHANES formalism also accounts for the feedback from both SNeII and BH accretion in determining the final gas mass at the end of any time-step; this acts as the initial gas mass for the next time-step in order to track the baryonic assembly of such early systems. Assuming perfect mixing of metals and gas, the formalism accounts for the key processes of metal production (where the latest mass-dependent stellar yields from C. Kobayashi et al. 2020 are used), astration into BH accretion and star formation, and loss in BH- and SNII-powered outflows in order to calculate the metal enrichment of these early systems.

G5 PBH hydrodynamical simulations

Using cosmological *N*-body and hydrodynamic simulations with the GIZMO code (P. F. Hopkins 2015), we model the formation of the first galaxies in PBH-seeded haloes, taking into account the accretion and feedback of an isolated PBH with $5 \times 10^7\,\mathrm{M}_\odot$, placed in a simulation box of comoving size $L \sim 1\,\mathrm{Mpc}\,h^{-1}$. This PBH mass scale could arise from an initial $\sim 10^6\,\mathrm{M}_\odot$ seed, related to the e^+e^- phase transition in the ultra-early Universe (e.g. B. Carr et al. 2021), and assuming subsequent growth through the merger of clustered PBHs in a highly biased region. To simulate the formation of structure around the PBH, we adopt the numerical recipes summarized in S. Zhang et al. (2025), to which we refer for further details. The simulations are run to $z \sim 7$, when QSO1 is observed. We specifically implement a star formation prescription for Jeans unstable gas in the vicinity of an accreting PBH, taking into account the intricate interaction between the different gaseous components.

The accretion-driven growth of the PBH is sensitive to the coupling strength of the accretion-generated luminosity, $L_{\rm BH}$, to the surrounding gas, implemented via thermal energy injection: $\delta E = \epsilon_r L_{\rm BH} \delta t$, given a simulation time-step δt. In this case, we take a fiducial value of $\epsilon_r \sim 0.5$ per cent, following S. Zhang et al. (2025). By $z \sim 7$, feedback heating of the ambient gas suppresses efficient accretion and further growth, resulting in a final BH mass of $M_{\rm BH} \simeq 6 \times 10^7\,\mathrm{M}_\odot$ and delayed build-up of stellar mass, yielding $M_{\rm star} \sim 2 \times 10^7\,\mathrm{M}_\odot$ – both comparable to current observational estimates for QSO1. The (radiation-hydrodynamical) gas flows in the vicinity of the accreting PBH, however, are complex, and follow-up simulations are required to determine the branching ratio of such large-scale inflows into feeding of the BH and of the concurrent starburst, covering a statistically representative sample of environments.

We track the metallicity evolution in galaxies by post-processing, incorporating both star formation and gas outflows driven by BH feedback. The metallicity Z of a galaxy at a given time t is estimated as the ratio of metal mass $M_Z(t)$ to gas mass $M_{\rm gas}(t)$, contained within the outflow bubble:

$$Z(t) = \frac{M_Z(t)}{M_{\rm gas}(t)}\,, \tag{G2}$$

assuming a uniform distribution within this bubble and ignoring metal diffusion at the bubble surface.

The metal mass is given by

$$M_Z(t) = \mathcal{M}_Z M_{\rm star}(t)\,, \tag{G3}$$

where $M_{\rm star}(t)$ is the stellar mass as a function of cosmic time, and $\mathcal{M}_Z$ is the metal yield per unit stellar mass, which depends on the stellar initial mass function (IMF) and stellar evolution models for winds and SNe. Based on the stellar evolution models in G. Costa & others (2025), we estimate $\mathcal{M}_Z$ to be in the range $\sim 0.02 - 0.19$, bracketing the plausible range for different IMFs (from present-day to Pop III stars).

We estimate the size of the outflow bubble as the radius where the average outflow velocity drops below the local sound speed, and further simplify our model by neglecting the delay between star formation and subsequent metal enrichment due to stellar evolution. Fig. 5(d) shows a representative trajectory for the resulting metallicity evolution with the initial conditions described above. By $z \sim 7$, the metallicity is estimated to lie within $Z/Z_\odot \sim 0.002 - 0.02$, consistent with what is observed for QSO1. We again refer to S. Zhang et al. (2025) for a detailed description of the numerical implementation and simulation parameters. We note, however, that this post-processed enrichment model remains an approximation; a more complete treatment incorporating explicit stellar evolution and metal enrichment recipes will be explored in an upcoming work.

[1]*Kavli Institute for Cosmology, University of Cambridge, Madingley Road, Cambridge CB3 0HA, UK*
[2]*Cavendish Laboratory, University of Cambridge, 19 JJ Thomson Avenue, Cambridge CB3 0HE, UK*
[3]*Department of Physics and Astronomy, University College London, Gower Street, London WC1E 6BT, UK*
[4]*Max-Planck-Institut für Extraterrestrische Physik, Gießenbachstraße 1, D-85748 Garching, Germany*
[5]*Centro de Astrobiología (CAB), CSIC-INTA, Cra. de Ajalvir Km. 4, E-28850 Torrejón de Ardoz, Madrid, Spain*
[6]*Department of Astronomy, University of Texas at Austin, Austin, TX 78712, USA*
[7]*Weinberg Institute for Theoretical Physics, Texas Center for Cosmology and Astroparticle Physics, University of Texas at Austin, Austin, TX 78712, USA*
[8]*Canadian Institute for Theoretical Astrophysics, 60 St George St, University of Toronto, Toronto, ON M5S 3H8, Canada*
[9]*St Catharine's College, University of Cambridge, Trumpington Street, Cambridge CB2 1RL, UK*
[10]*Institute of Astronomy, University of Cambridge, Madingley Road, Cambridge CB3 0HA, UK*
[11]*Center for Computational Astrophysics, Flatiron Institute, 162 Fifth Avenue, New York, NY 10010, USA*
[12]*Centre for Astrophysics Research, Department of Physics, Astronomy and Mathematics, University of Hertfordshire, College Lane, Hatfield AL10 9AB, UK*
[13]*Universität Heidelberg, Zentrum für Astronomie, Institut für Theoretische Astrophysik, D-69120 Heidelberg, Germany*
[14]*Dipartimento di Fisica, 'Sapienza' Università di Roma, Piazzale Aldo Moro 2, I-00185 Roma, Italy*
[15]*INAF/Osservatorio Astronomico di Roma, Via di Frascati 33, I-00040 Monte Porzio Catone, Italy*
[16]*INFN, Sezione Roma1, Dipartimento di Fisica, 'Sapienza' Università di Roma, Piazzale Aldo Moro 2, I-00185 Roma, Italy*
[17]*Sapienza School for Advanced Studies, Viale Regina Elena 291, I-00161 Roma, Italy*
[18]*Como Lake Center for Astrophysics, DiSAT, Università degli Studi dell'Insubria, via Valleggio 11, I-22100 Como, Italy*
[19]*Sorbonne Université, CNRS, UMR 7095, Institut d'Astrophysique de Paris, 98 bis bd Arago, F-75014 Paris, France*
[20]*Kavli Institute for Astronomy and Astrophysics, Peking University, Beijing 100871, China*
[21]*Scuola Normale Superiore, Piazza dei Cavalieri 7, I-56126 Pisa, Italy*
[22]*Institute of Liberal Arts and Science, Kanazawa University Kakuma Kanazawa, Ishikawa 920-1192, Japan*
[23]*Waseda Research Institute for Science and Engineering, Faculty of Science and Engineering, Waseda University, 3-4-1, Okubo, Shinjuku, Tokyo 169-8555, Japan*
[24]*Cosmic Dawn Center (DAWN), Copenhagen, Denmark*

[25]*Niels Bohr Institute, University of Copenhagen, Jagtvej 128, DK-2200, Copenhagen, Denmark*
[26]*Department of Physics, University of Oxford, Denys Wilkinson Building, Keble Road, Oxford OX1 3RH, UK*
[27]*European Southern Observatory, Karl-Schwarzschild-Strasse 2, 85748 Garching, Germany*
[28]*Università di Firenze, Dipartimento di Fisica e Astronomia, via G. Sansone 1, I-50019 Sesto Fiorentino, Florence, Italy*
[29]*INAF – Arcetri Astrophysical Observatory, Largo E. Fermi 5, I-50125, Florence, Italy*
[30]*Department of Astronomy & Astrophysics, University of Chicago, 5640 S Ellis Avenue, Chicago, IL 60637, USA*
[31]*Kavli Institute for Cosmological Physics, University of Chicago, Chicago IL 60637, USA*
[32]*AURA for European Space Agency, Space Telescope Science Institute, 3700 San Martin Drive. Baltimore, MD 21210, USA*
[33]*Aix Marseille Université, CNRS, CNES, LAM (Laboratoire d'Astrophysique de Marseille), UMR 7326, F-13388 Marseille, France*
[34]*Department of Astronomy and Astrophysics, University of California, Santa Cruz, 1156 High Street, Santa Cruz, CA 96054, USA*
[35]*Center for Astrophysics | Harvard & Smithsonian, 60 Garden St., Cambridge, MA 02138, USA*

This paper has been typeset from a TEX/LATEX file prepared by the author.